THESIS APPROVAL

GRADUATE SCHOOL, KASETSART UNIVERSITY

Master of Engineering (Electrical Engineering)

DEGREE

Electrical Engineering	Electrical Engineering
FIELD	**DEPARTMENT**

TITLE: Fusion of Hyperspectral and Multispectral Images

NAME: Mr. Tanakorn Sritarapipat

THIS THESIS HAS BEEN ACCEPTED BY

THESIS ADVISOR

(Assistant Professor Teerasit Kasetkasem, Ph.D.)

THESIS CO-ADVISOR

(Mr. Ekachai Phaisangittisagul, Ph.D.)

DEPARTMENT HEAD

(Associate Professor Vichai Surapatana, Ph.D.)

APPROVED BY THE GRADUATE SCHOOL ON _____

DEAN

(Associate Professor Gunjana Theeragool, D.Agr.)

THESIS

FUSION OF HYPERSPECTRAL AND MULTISPECTRAL IMAGES

TANAKORN SRITARAPIPAT

A Thesis Submitted in Partial Fulfillment of
the Requirements for the Degree of
Master of Engineering (Electrical Engineering)
Graduate School, Kasetsart University
2011

Tanakorn Sritarapipat 2011: Fusion of Hyperspectral and Multispectral Images. Master of Engineering (Electrical Engineeing), Major Field: Electrical Engineeing, Department of Electrical Engineering. Thesis Advisor: Assistant Professor Teerasit Kasetkasem, Ph.D. 67 pages.

The objective of this thesis is to develop an image fusion algorithm for combining a low-resolution hyperspectral image with a high-resolution multispectral image to obtain a high spatial resolution hyperspectral image. To achieve this goal, we investigate therelationship between low-resolution hypersectral data and high-resolution multispectral data, and the spatial correlation of the corresponding data from neighboring pixels. The proposed algorithm is based on a statistical model and employs the maximum *a posteriori* (MAP) estimator for enhancing the spatial and spectral resolutions. The Huber Markov random field (Huber-MRF) is used to preserve the spatial correlation in the fused data. A closed-form solution to find the fused hyperspecral images is also derived here. Experiments results with hyperspectral and multispectral images acquired from Small Multi-Mission Satellite (SMMS) (HJ-1A) show that the proposed fusion algorithm works effectively in fusing hyperspectral and multispectral images.

/ /

Student's signature Thesis Advisor's signature

ACKNOWLEDGEMENTS

I would like to express my grateful thank and deeply indebted to Asst. Prof. Dr. Teerasit Kasetkasem my thesis advisor, and Dr. Ekachai Phaisangittisagul my co-advisors, encouragement and valuable suggestion for completely writing of thesis.

This research is financially supported by The Center of Promoting Research and Development of Satellite Image Application in Agriculture, Kasetsart University. We also would like to thank NTC Telecommunication Research Laboratory at Department of Electrical Engineering, Kasetsart University for Matlab program.

Tanakorn Sritarapipat
April 2011

TABLE OF CONTENTS

Page

LIST OF TABLES

LIST OF FIGURES

LIST OF FIGURES (Continued)

LIST OF FIGURES (Continued)

LIST OF FIGURES (Continued)

LIST OF ABBREVIATIONS

CRESDA	=	China centre for resource satellite data and application
Huber-MRF	=	Huber-Markov random field
MAP	=	Maximum *a posteriori*
NTC	=	National Telecommunications Commission
RMSE	=	Root mean square error
SAM	=	Spectral angle mapper
SMMS	=	Small multi-mission satellite
SNR	=	Signal to noise ratio
UIQI	=	Universal image quality index

FUSION OF HYPERSPECTRAL AND MULTISPECTRAL IMAGES

INTRODUCTION

Nowadays, the use of remote sensing images has received a great deal of attentions. In the market, many applications such as vegetation mapping, environmental monitoring, mineral mapping, oil exploration, hydrology, tsunami-aids and agriculture yield prediction cannot be successful without the information provided by some remote sensing images. The increase in the utilization of remote sensing data is due to the availability of high quality images with a reasonable cost and improvement in the cheap computational power. With the current imaging systems, the demands for higher spatial and spectral precision data to generate even more spatial detail map with many different land cover classes are still on the rise. This increasing demand forces the system designer to create higher spectral and spatial resolution of remotely sensed imagery. These requirements can be either fulfilled by building new satellites with a superior resolution power, or by the utilization of image processing techniques. The main advantage of the second alternative is the lower cost. This technique often involves the fusion of images from different sources, acquired at different times, or having different characteristics.

The fusion of multi-sensor image data is a widely used procedure for complementing and enhancing the information extraction. The high-spatial resolution data are important in terms of getting the shape, size and orientation of the different features while high-spectral resolution data are needed in terms of spectrally distinguishing each and every pixel for classification and feature extraction. When high spatial resolution data are merged with the high spectral resolution data, the fused product obtained is better in spatial and spectral resolution.

The fusion of multispectral and panchromatic images had been done in past by several researchers for different purposes. Nevertheless, in the recent years, the fusion

of hyperspectral and multispectral images is the latest approach to acquire significant and reliable information that cannot be acquired with fusion of multispectral and panchromatic images. The main distinction between fused hyperspectral images with multispectral images and fused multispectral images with panchromatic images is usually the number of spectral bands. The fused multispectral data contains from several to tens of bands. The fused hyperspectral data contains dozens to hundreds of bands. Thereby the fused hyperspectral images have more spectral resolution than the fused multispectral images hence it should be arrange significant and reliable information. However, the drawback of this approach provides complex solution.

This thesis provides an introduction to new technique for the fusion of hyperspectral and multispectral images.

OBJECTIVES

Developing a new algorithm to fuse hyperspectral and multispectral images to obtain hyperspcetral image with high spatial resolution as multispectral image.

LITERATURE REVIEW

The fusion of multispectral and panchromatic images has been widely studied for decades. One of the most popular approaches is to use intensity–hue–saturation (IHS) transform, (Carper et al., 1990). The most important steps are: (1) Transforming a color image composite from the RGB space into the IHS space; (2) Replacing the intensity component by a panchromatic image with a higher resolution; and (3) Reversing the transformation by replacing components from IHS space back to the original RGB space to obtain a fused image. The IHS method distorts the spectral characteristics of the fused data because the underlying assumption that the panchromatic image is the summation of images from all spectral bands may be invalid due to the panchromatic sensor response. Moreover, the IHS method has one major limitation, i.e., only three bands can be merged at any one time.

The principal component analysis (PCA), proposed by Chavez and Kwarteng (Chavez and Kwarteng, 1989), is similar to the process in the IHS method. The steps are: (1) Performing a principal component transformation to convert a set of multispectral bands (three or more bands) into a set of principal components; (2) Replacing one principal component, usually the first component, by a high resolution panchromatic image; and (3) Performing a backward principal component transformation to convert the replaced components back to the original image space. The PCA method still introduces some distortion to the spectral characteristics of the fused data, but the distortions are less than those in the IHS method since the first principle component image is constructed more similar the construction of panchromatic image than the intensity image because the results of the PCA method are better than the IHS Method. Another advantage of the PCA over the IHS method is that the PCA method can fuse the panchromatic data with all the multispectral bands at the same time. Also, if subgroups of three bands are used, the resulting first principal component images are more highly correlated with each other than in the intensity images generated from these same data (Chavez and Kwarteng, 1989). This

confirms the assumption that the panchromatic data are similar to the first principal component data remains semiconstant regardless of the subgroup combination.

The Brovey transform, (Civco et al., 1995) is another method for fusing multispectral and panchromatic data together. The Brovey transform employs the addition, division and multiplication for the fusion of three multispectral bands. Its basic processing steps are: (1) Adding three multispectral bands together to create the sum image; (2) Dividing each multispectral band by the sum image; and (3) Multiplying each quotient by a high resolution panchromatic. With the Brovey transform, it is necessary to select only three subbands. In general, the pixel grey values are smaller than those of other fusion techniques. The color distortion is obvious and varies depending on the band combinations being fused.

The algorithm used filtering is the high-pass filtering (HPF) method, proposed by Shettigare (Shettigare, 1992). In the HPF method, the higher spatial resolution data have a small kernel size of high-pass spatial filter applied. The results of the small kernel size of high-pass filter contain the high-frequency component that is related mostly to spatial information. The spatial filter removes most of the spectral information. The HPF results are added, pixel by pixel, to the lower spatial resolution but higher spectral resolution. This method has the minimum distortion in term of the spectral characteristics of the data. In the HPF method, the spatial filter results can be used on one or all the spectral bands. A possible problem is the slight ringing caused by the spatial filter at high contrast boundaries.

The widely method used in software is the Gram-Schmidt (GS) transformation based the concept of the panchromatic sharpening method, (Laben and Brower, 2000). This method was implemented in the Environment for Visualizing Images (ENVI) commercial software package.

Multi-resolution analysis based algorithms such as a discrete-wavelet-transform (DWT), (Zhou et al., 1998) has received a great deal of attention lately. The wavelet based fusion is performed in the following way: (1) Decomposing a high

resolution panchromatic image into a set of low resolution panchromatic images with wavelet coefficients for each level; (2) Replacing a low resolution panchromatic with a multispectral band at the same resolution level; and (3) Performing a backward wavelet transformation to convert the decomposed and replaced panchromatic set back to the original panchromatic resolution level. A major limitation of the wavelet based fusion is the high computational requirement because it extracts spatial details from a high-resolution panchromatic image, and then adds them into the multispectral bands. In this manner, the color distortion can be reduced to a certain extent, but the fused image appears similar to the result of a high-pass filtering fusion, i.e.., the spectral color may not be smoothly integrated into the spatial features. Next, the discrete wavelet frame transform (DWFT), introduced by Li (Li et al., 2002), propose a pixel level image fusion algorithm for merging Landsat thematic mapper (TM) images and SPOT panchromatic images. The two source images are first decomposed using the discrete wavelet frame transform (DWFT), which is both aliasing free and translation invariant. Wavelet coefficients from TM's approximation subband and SPOT's detail subbands are then combined together, and the fused image is reconstructed by performing the inverse DWFT. Experimental results (Li et al, 2002) has shown that discrete wavelet transform method preserve spectral and spatial information, especially in situations where the source images are not perfectly registered.

Next method is multispectral image data fusion using projection onto convex sets (POCS) and super-resolution (Aguena and Mascarenhas, 2006). They want to combine the characteristics of multispectral (better spectral definition) and panchromatic (better space definition) images. The process proposes solutions using projection onto convex sets (POCS) techniques divided in two steps: (1) regularizing the block artifacts and using super-resolution techniques based on POCS and (2) synthesizing multispectral image obtained by sequential and parallel projections or by the least squares method.

Another method is image fusion algorithm based on restoration. (Li and Leung, 2009). The wavelength of the panchromatic band usually covers the

wavelengths of the multispectral bands. This relationship between the two kinds of images is useful for fusion. In their approach, the low-resolution multispectral images are first resampled to the scale of the high-resolution panchromatic image. The relationship between these two kinds of images is then used to restore the resampled multispectral images. That is, the resampled multispectral images are modeled as the noisy blurred versions of the ideal multispectral images, and the high-resolution panchromatic image is modeled as a linear combination of the ideal multispectral images plus the observation noise. The ideal high-resolution multispectral images are then estimated based on the panchromatic and the resampled multispectral images.

The fusions of hyperspectral and multispectral images have recently been proposed. Where multi-resolution analysis based algorithms are employed. Commonly used multi-resolution analysis is 2-D wavelet based method, (Gomez et al., 2001) is similar to the concept of wavelet image fusion between panchromatic and multispectral images but use different approach. Furthermore, another multi-resolution analysis is based on the 3-D wavelet transformation, (Yifan and Mingyi, 2007). This method uses 3-D analysis instead of traditional 2-D analysis. The 3-D analysis is believed by Yifan and Mingyi to be more suitable since the 3-D wavelet transformation can utilize both spatial and spectral characteristics of source images more adequately and produce fused image with higher quality and fewer artifacts than fusion approach using 2-D wavelet transformation. Hence, it is capable of maintaining the spatial and spectral characteristics more effectively.

Another approach is based on statistical model. This technique uses maximum *a posteriori* (MAP) estimation for enhancing hyperspectral imagery (Hardie et al., 2004). They focus on the use of high-resolution panchomatic data or high-resolution multispectral data to enhance hyperspectral imagery. The proposed technique is suitable for applications where some correlation, either localized or global, exists between the auxiliary image and the image being enhanced. The technique naturally works in the spatial domain but also works in the wavelet domain for redundancy hyperspectral imagery (Zhang et al., 2008).

There are several researches for specific purpose such as for urban areas; the fusion of hyperspectral and radar data using the HSI transformation (Chena et al., 2003). The Intensity–Hue–Saturation (IHS) transformation is used to integrate the high spectral resolution, provided by hyperspectral data and the surface texture information, derived from radar data into a single image of an urban area. The fusion of spectral and shape features using reflective and thermal hyperspectral data (Segl et al., 2003) has been extended to a shape-based classification technique including the thermal bands of the DAIS instrument to improve the detection of buildings during the process of identifying seedling pixels, which represent the starting points for linear spectral unmixing. This approach increases the reliability of differentiation between buildings and open spaces, leading to more accurate results for the spatial distribution of surface cover types. For coastal mapping; Fusion of hyperspectral images and lidar-based dems, (Elaksher, 2008). The DEM was used to detect and create a vector layer for building polygons. Subsequently, building pixels were removed from the AVIRIS image and the image was classified with a supervised classifier to discriminate road and water pixels. Two vector layers for the road network and the shoreline segments were vectorized from road pixels and water-body border pixels using several image-processing algorithms. Utilizing laser ranging data to detect and remove buildings from optical images before the classification process enhances the outcomes. Consequently, integrating laser and optical data provides high-quality and more reliable coastal geospatial information.

MATERIALS AND METHODS

Materials

1. Personal Computer
2. MATLAB Simulation software
3. Microsoft Visual Studio (C++)
4. Hyperspectral and multispectral images acquired from Small Multi-Mission Satellite (SMMS) (HJ-1A) on December 19, 2008 and cover Suvarnabhumi Airport, Thailand

Methods

1. Research area and experimental setup

The fusion of hyperspectral and multispectral images is a process that merges high spectral resolution image (low-resolution hyperspectral image) with high spatial resolution image (high-resolution multispectral image) to produce fused image with high spatial and spectral resolutions (high-resolution hyperspectral image). In this thesis, we focus on the relationship between low-resolution hypersectral data and high-resolution multispectral data, and the spatial correlation of digital number vectors among neighboring pixels. The proposed technique is based on a statistical model and employs the maximum *a posteriori* (MAP) estimator (Kay, 1993) for enhancing the spatial and spectral resolution. The Huber Markov random field (Huber-MRF) is used to preserve the spatial correlation in the fused data (Pan and Reeves, 2006).

The HJ1-A satellite in the small multi-mission satellites (SMMS) acquired remotely sensed images for our experiments. The orbit parameter is given in Table 1. The HJ1-A satellite has two sensors, the hyperspectral imager sensor having 115-128 contiguous spectral bands in the range from 0.45 to 0.95 μm (shown in Appendix),

and the CCD camera sensor having four spectral bands in the range from 0.43 to 0.90 μm (Table 2). In our experiment, a hyperspectral image (Figure 1) with 115 bands at the spatial resolution of 100 meters acquired on December 19, 2008, and multispectral image (Figure 2) with 4 bands at the spatial resolution of 30 meters acquired on December 19, 2008. These images cover Suvarnabhumi Airport, Thailand

Table 1 Orbital characteristics of CBERS-02B of HJ-1A satellite

Satellite	HJ-1A
Orbit	Sun synchronous recurrent frozen orbit
Altitude	650 km
Inclination	97.95 degree
Repetition cycle	31 days
Descending node (local time)	10:30 AM
On-board capacity	16 Gbits

Table 2 Technical specification of payload of HJ-1A

Satellite	Payload	Band no.	Spectral range (μm)	Spatial resolution (m)	Swath width (km)	Side-looking ability	Repetition cycle (days)	Data transmission rate (Mbps)
HJ-1A	CCD Camera	1	0.43-0.52	30	700		4	120
		2	0.52-0.60	30				
		3	0.63-0.69	30				
		4	0.76-0.9	30				
	Hyper spectral imager	1-110, 128	0.45-0.95	100	50	30	4	120

Tables 1 and 2 are provided from CRESDA (China centre for resource satellite data and application) (source: http://www.cresda.com/n16/n92006/n92066/n98627/index.html, September 17, 2010)

Figure 1 False color composite of the hyperspectral image size of 300x300 pixels and 115 bands covering Suvarnabhumi Airport (Blue:20th band, Green: 50th band, and Red: 100th band)

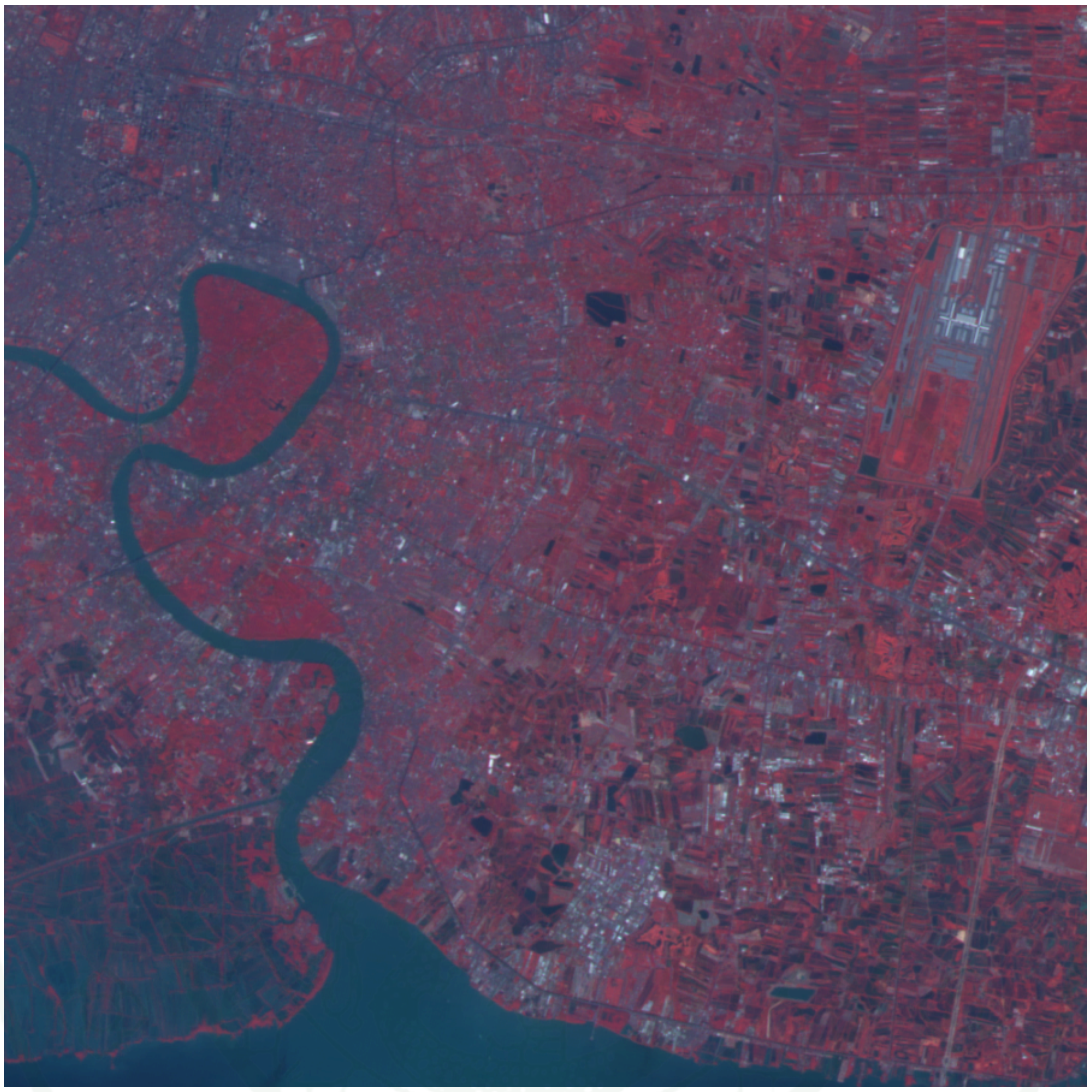

Figure 2 False color composite of the multispectral image size of 1000x1000 pixels and 115 bands covering Suvarnabhumi Airport (Blue: 1st band; Green: 2nd band; and Red: 4th band)

2. Observation Model

The observation model can be described as the fusion of a low-resolution hypersepctral image Y having P bands and M pixels per band and a high-resolution multispectral image X having Q bands and N pixels per band to fused a high-resolution hypersepctral image Z having P bands and N pixels per band ($M<N$ and $Q<P$)

The high-resolution multispectral image data-cube in band-interleaved-by-pixel will be denoted

$$\mathbf{x} = [x_{1,1}, \dots, x_{Q,1}, x_{1,2}, \dots, x_{Q,2}, \dots, x_{1,N}, \dots, x_{Q,N}]^T \quad (1)$$

where $\mathbf{x_n} = [x_{1,n}, x_{2,n}, \dots, x_{Q,N}]^T$ represents the high-resolution multispectral image at Pixel n, for n = 1,2,…,N. The vectors, $\mathbf{x}_n$, will be referred to as high-resolution multispectral pixels.

The low-resolution hyperspectral image having P bands and M pixels per band is denoted

$$\mathbf{y} = [y_{1,1}, \dots, y_{P,1}, y_{1,2}, \dots, y_{P,2}, \dots, y_{1,M}, \dots, y_{P,M}]^T \quad (2)$$

where $\mathbf{y}_m = [y_{1,m}, y_{2,m}, \dots, y_{P,m}]^T$ represents the low-resolution hyperspectral image at pixel m, for m = 1,2,…,M. The vectors, $\mathbf{y}_m$, will express in terms of low-resolution hyperspectral pixels.

The desired high-resolution hyperspectral image will be denoted

$$\mathbf{z} = [z_{1,1}, \dots, z_{P,1}, z_{1,2}, \dots, z_{P,2}, \dots, z_{1,N}, \dots, z_{P,N}]^T \quad (3)$$

where $\mathbf{z}_n = [z_{1,n}, z_{2,n}, \dots, z_{P,N}]^T$ represents the high-resolution hyperspectral image at

pixel n, for $n = 1,2,...,N$. The vectors, $\mathbf{z}_n$, will express in terms of high-resolution hyperspectral pixels.

The relationships among these images are divided into four parts. In the first part, we model the relationship between high spatial resolution multispectral and hyperspectral images. To achieve this goal, we begin by plotting the idea spectral responses of both hyperspectral and multispectral sensors. Here, we observe that all the bands of hyperspectral sensors are roughly covered by spectral band of a multispectral sensor. On another hand, the multispectral data in a band can be written as a linear combination of spectral responses of hyperspectral data occupying the same wavelength interval; i.e.,

$$\mathbf{x} = \mathbf{A}\,\boldsymbol{z} + \boldsymbol{\mu} + \mathbf{n} \tag{4}$$

where $\mathbf{x}$ is a digital number vector of multispectral pixel, $\boldsymbol{z}$ is a digital number vector of the high-resolution hyperspectral pixel, $\mathbf{A}$ is a coefficient matrix of a potentially wavelength-dependent, and $\boldsymbol{\mu}$ is an offset vector, and $\mathbf{n}$ is an independent noise vector. From a sensor specification, we know that many wavelength hyperspectral bands are covered by one band of multispectral band. As a result, the coefficient matrix, $\mathbf{A}$, can be estimated directly from the observed spectral values in the corresponding homogenous regions from multispectral and hyperspectral images.

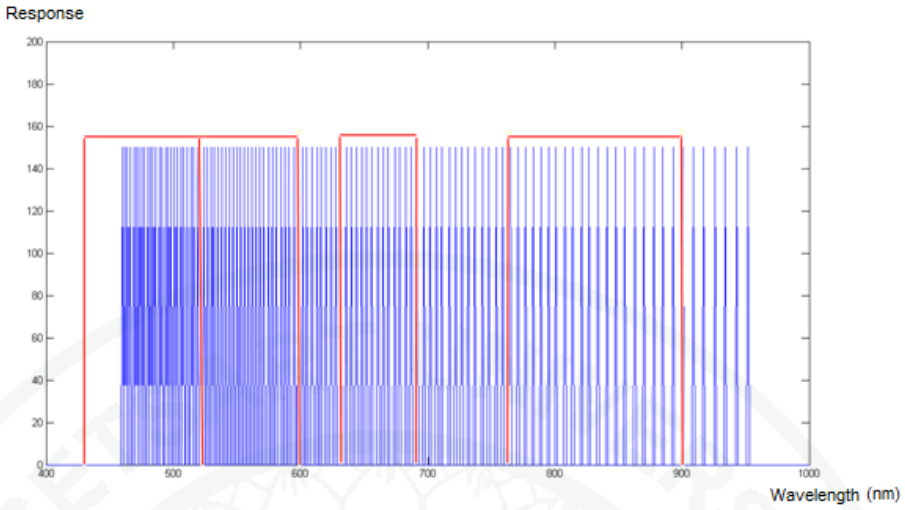

Figure 3 Ideal Spectral response of SMMS HJ-1A (Blue line is hyperspectral band and Red box is multispectral band)

In the second part, we focus on the relationship between a low-resolution and a high-resolution hyperspectral images. Figure 4 demonstrates the relationship between low- and high-resolution images. A pixel of a hyperspectral image at low resolution can be seen as a downsampling of a high resolution hyperspectral image. Hence, the resulting digital number at pixel in low resolution is equal to the average of digital numbers from the corresponding pixels in high-resolution, i.e.,

$$\mathbf{y_j} = \frac{1}{K}\sum_{i \in S_j} \mathbf{z_i} + \mathbf{e_j} \qquad (5)$$

where $\mathbf{y_j}$ is a digital number vector of low-resolution hyperspectral data at pixel j, $\mathbf{z_i}$ is a digital number vector of high-resolution hyperspectral data at pixel i, K is number of pixels of high resolution that covered a pixel of the low-resolution hyperspectral data (for simplicity, we assume K as an integer), and S_j is the set of pixels in high resolution hyperspectral image that cover the same area as pixel j is low resolution one. Finally, we assume that $\mathbf{e_j}$ is the independent measurement noise.

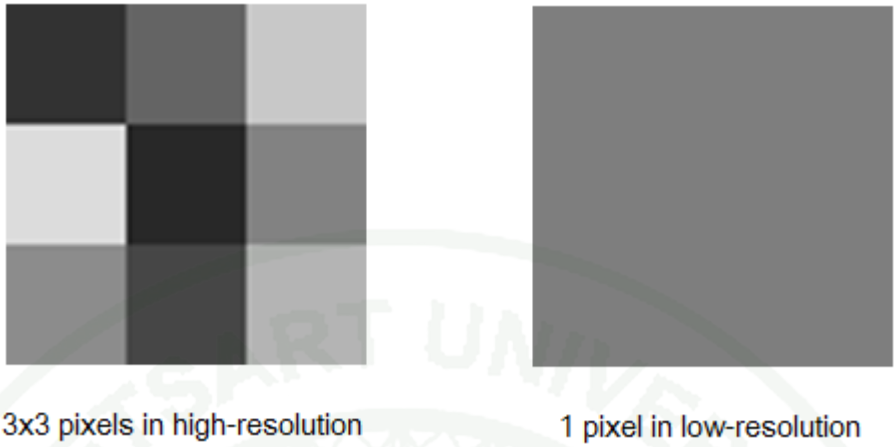

Figure 4 High resolution pixels and low resolution pixel at the same location

In the third part, the band to band relationship is considered. We investigate the relationship by plotting the digital numbers of a pixel from Bands 1 to 115 in Figure 5. The result shows that there a small differences between a digital number of a band and those of its neighboring band. In fact, the spectral response changes slowly from band to band.

$$\sum_{b=1}^{N_B-1}(z_{i,b}-z_{i,b+1})^2 = \mathbf{z}_i{}^{\mathrm{T}}\mathbf{B}\mathbf{z}_i \qquad (6)$$

where N_B is number of bands in hyperspectral image and **B** is

$$\begin{bmatrix} 1 & -1 & 0 & \cdots & & 0 \\ 0 & 1 & -1 & \cdots & & 0 \\ \vdots & \vdots & & \ddots & & \vdots \\ 0 & \cdots & & & 1 & -1 \end{bmatrix}^{\mathrm{T}} \begin{bmatrix} 1 & -1 & 0 & \cdots & & 0 \\ 0 & 1 & -1 & \cdots & & 0 \\ \vdots & \vdots & & \ddots & & \vdots \\ 0 & \cdots & & & 1 & -1 \end{bmatrix}$$

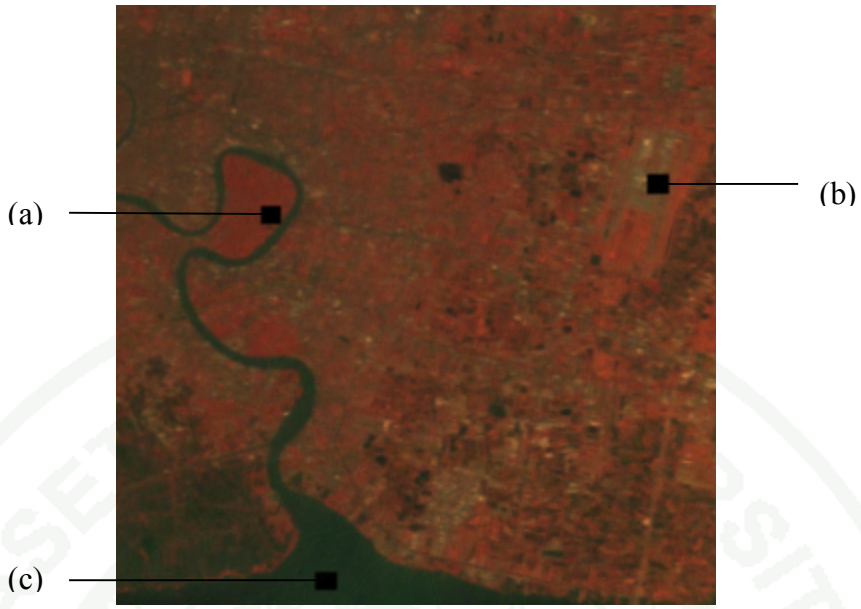

Figure 5 Hyperspectral image; (a) vegetation area (b) building area (c) water area

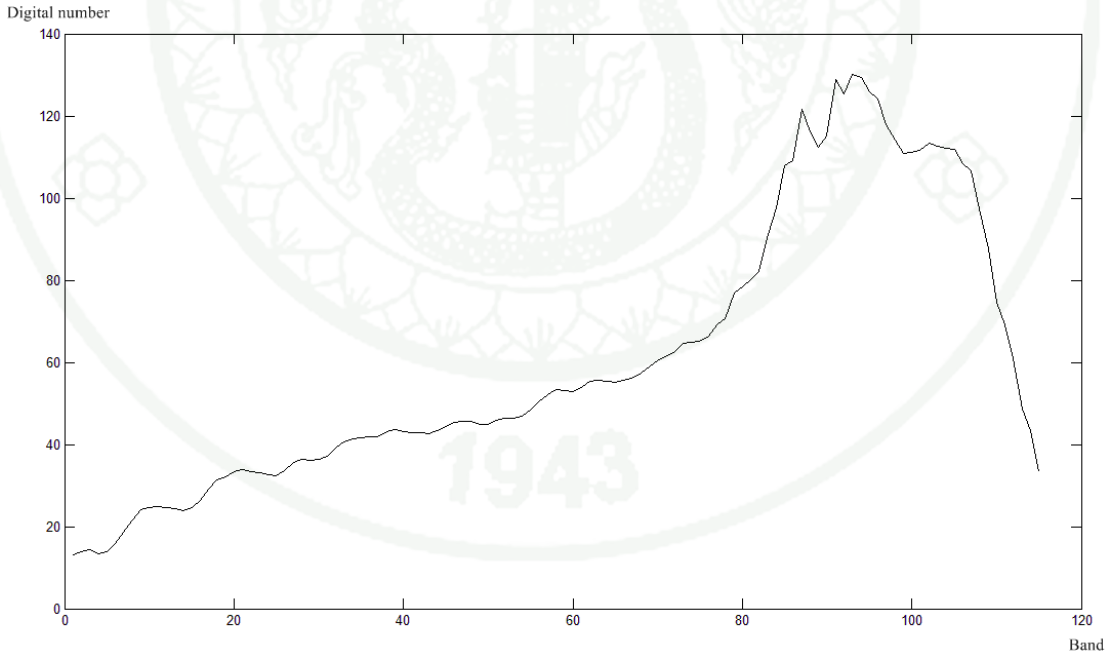

Figure 6 Digital number vector of hyperspectral pixel at pixel (100, 75) on vegetation area

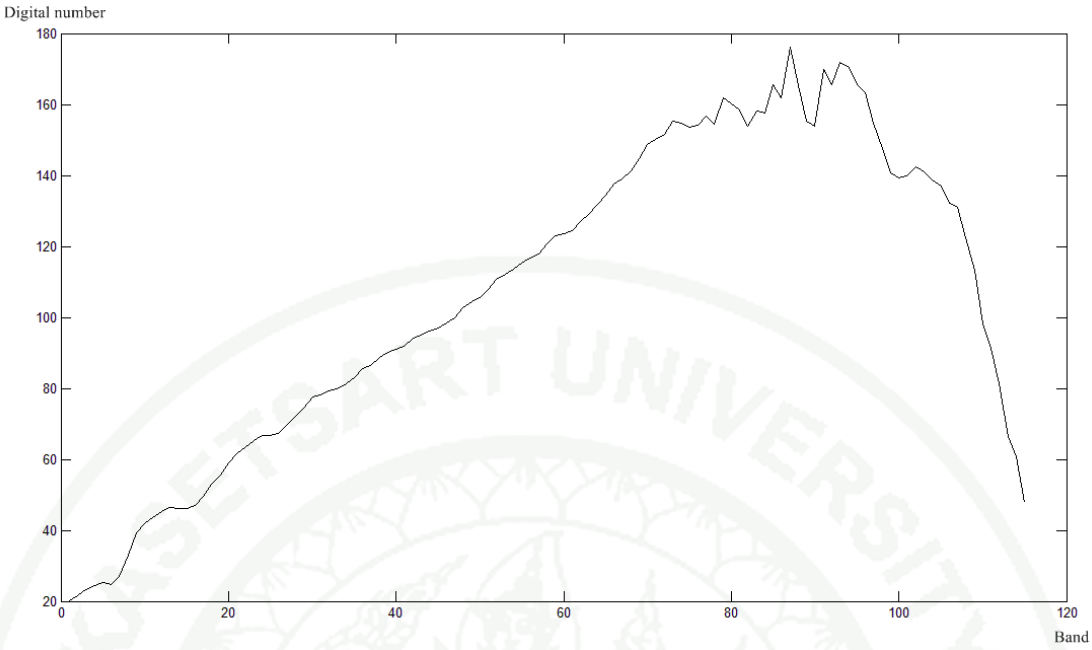

Figure 7 Digital number vector of hyperspectral pixel at pixel (90, 270) on building area

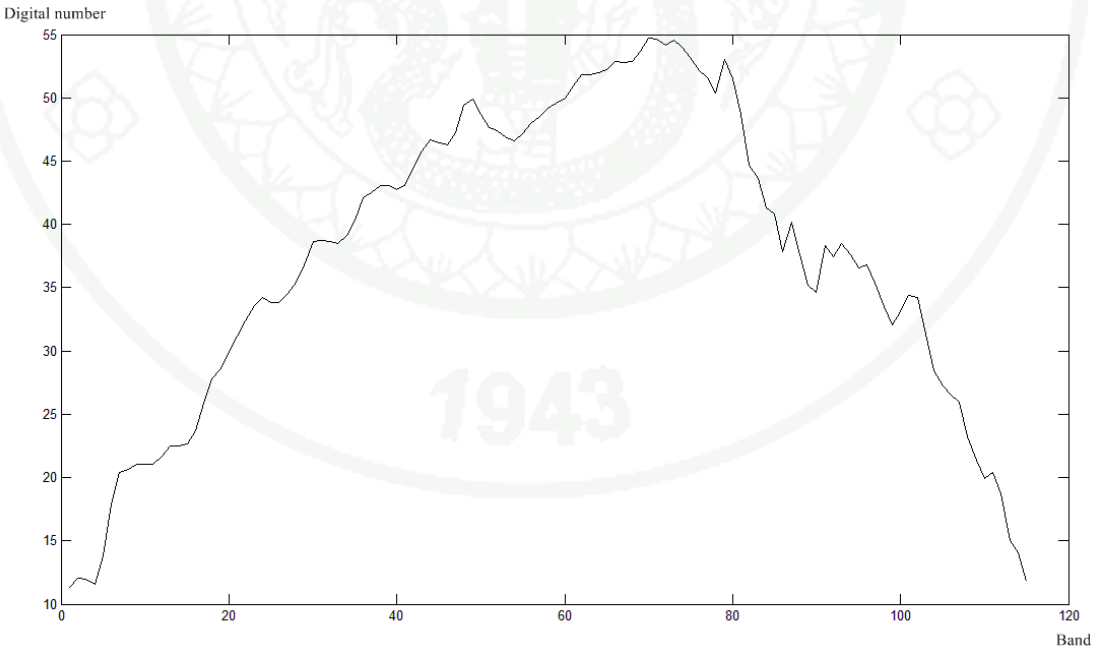

Figure 8 Digital number vector of hyperspectral pixel at pixel (285, 105) on water area

In the last part, we carry out the relationship of digital number vectors among neighboring pixels. Since the remotely sensed images are often taken over the homogenous or small heterogeneous regions. As a result, the observations from neighboring pixel are highly correlated. Figure 9 shows the digital numbers of a general image consisting of smooth and sharp areas. We investigate further on the hyperspectral image data by drawing horizontal lines (Figure 10) over three lines (the 100th, 200th, and 280th lines) over the 100th band. The digital numbers for all pixels on the lines are plotted in Figures 11-13 for the 100th, 200th, and 280th lines, respectively. The smooth area has roughly equal digital numbers among the neighboring pixels whereas the edges result in sharp jump or falls of the digital numbers. To capture this relationship, we model that the digital numbers among neighboring pixels as the Huber function (Huber, 1981) (Figure 14) which is defined as

$$\rho_T(x) = \begin{cases} x^2, & |x| < T \\ T^2 + 2T(|x| - T|), & |x| \geq T \end{cases} \tag{7}$$

where T is called Huber function threshold. The Huber function is convex and non-quadratic when $T<\infty$

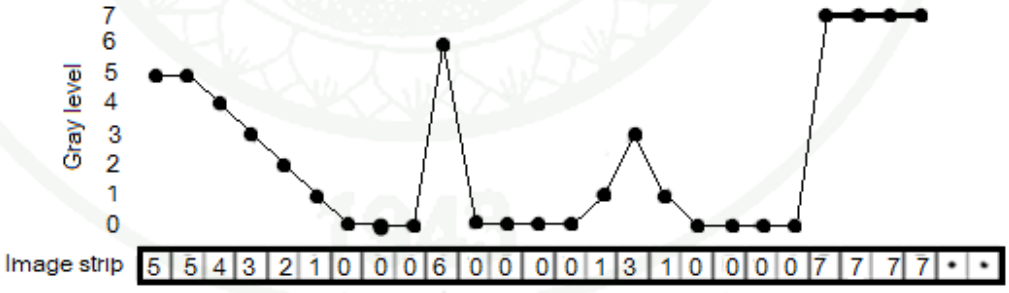

Figure 9 The intensity of each pixel in general image

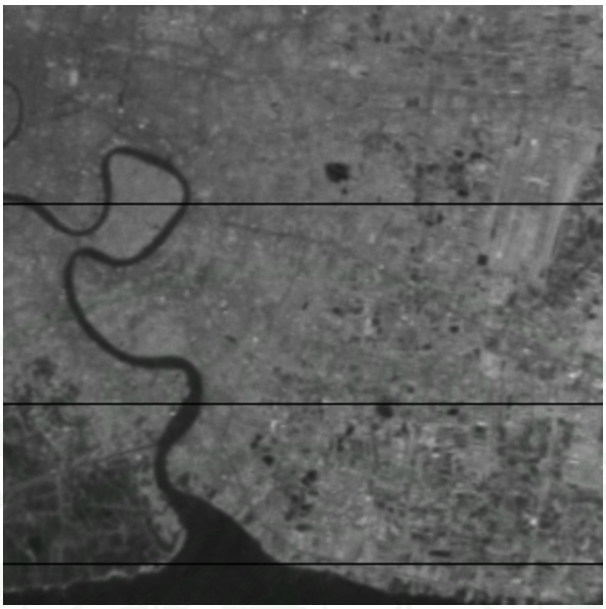

Figure 10 Hyperspectral image at band 100th ; (a) line 100 (b) line 200 (c) line 280

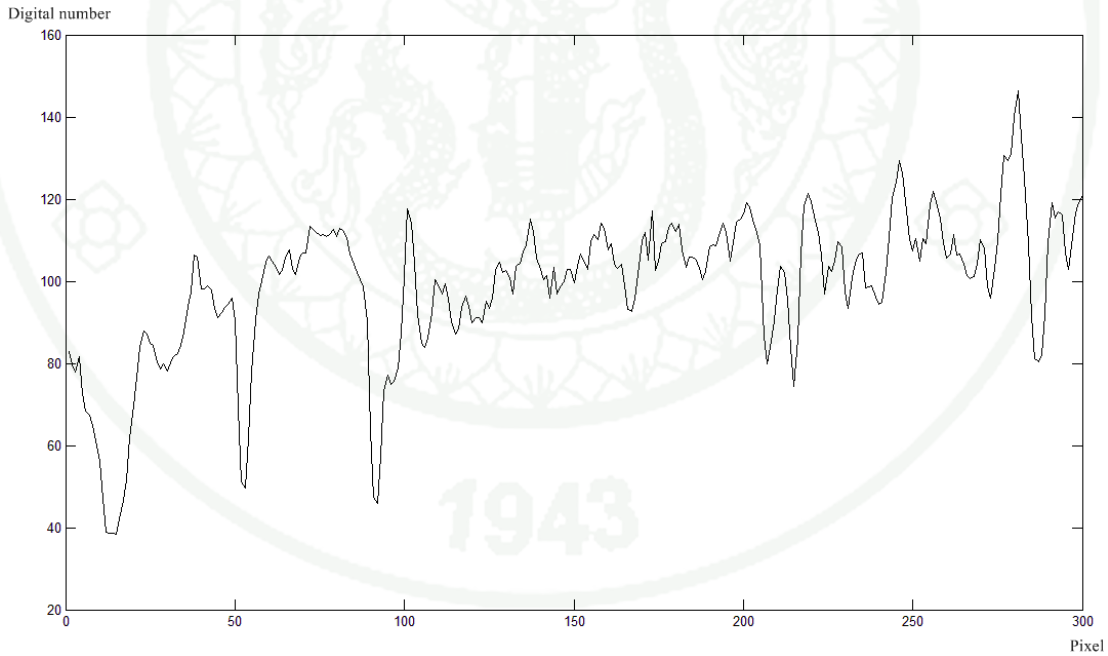

Figure 11 Digital number on line 100 in hyperspectral image at band 100th

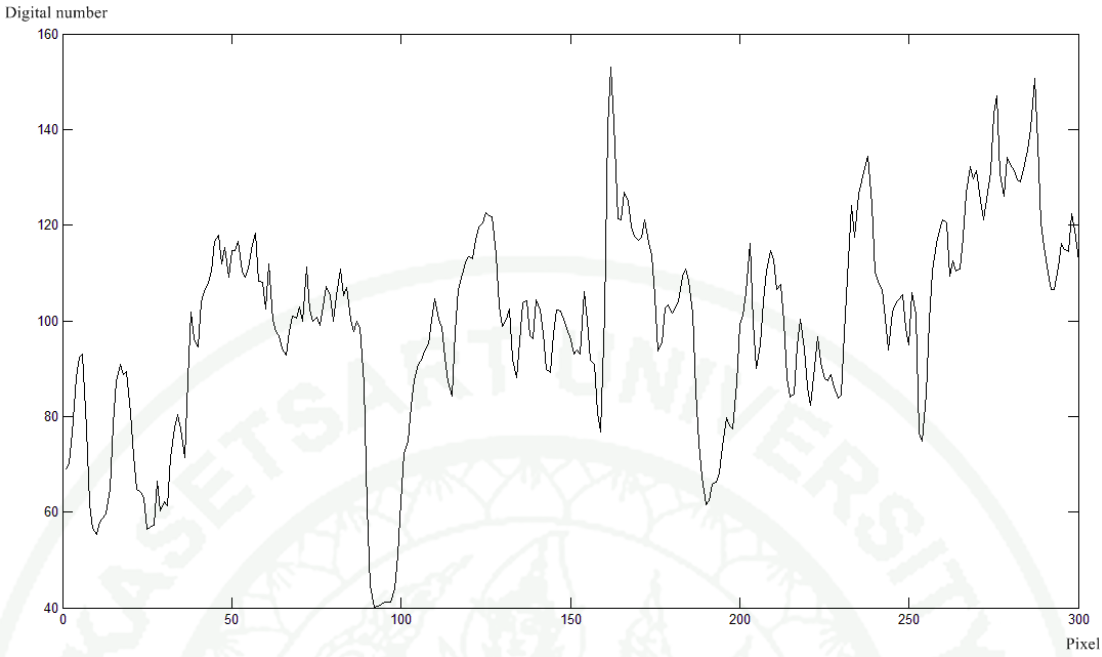

Figure 12 Digital number on line 200 in hyperspectral image at band 100th

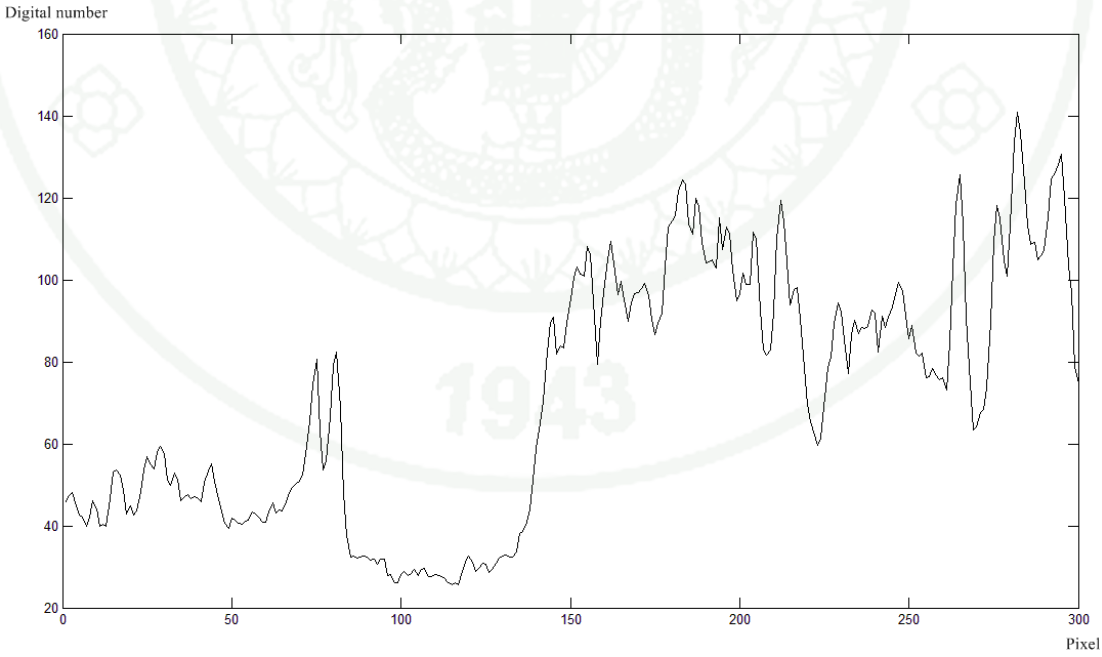

Figure 13 Digital number on line 280 in hyperspectral image at band 100th

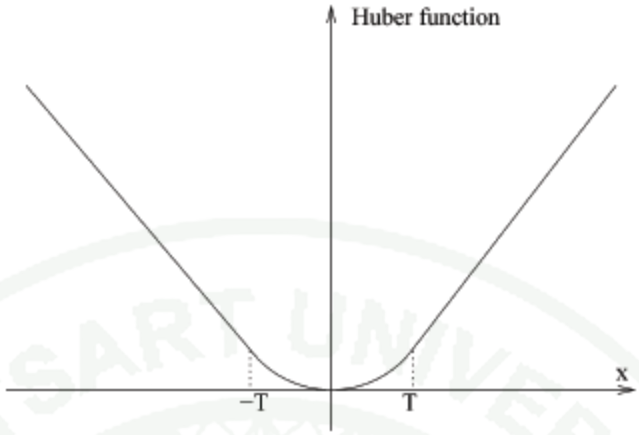

Figure 14 Huber function

3. Estimation Strategy.

In a statistical model, Z can be estimated from the conditional probability as a maximum *a posteriori* (MAP) estimation, when we can observe X and Y. Define as

$$\hat{Z} = \arg\ \max_Z \mathrm{P}(Z|X,Y) \tag{8}$$

where $\mathrm{P}(Z \mid X,Y)$ represents the conditional probability density function (pdf) of a high-resolution hyperspectral image given a high-resolution multispectral image and a low-resolution hyperspectral image. In other words, the MAP estimate find the most likely high resolution hyperspectral image that maximizes $\mathrm{P}(Z \mid X,Y)$. Using Bayes rule, we can write

$$\mathrm{P}(Z|X,Y) = \frac{\mathrm{P}(X,Y|Z)\mathrm{P}(Z)}{\mathrm{P}(X,Y)} \tag{9}$$

Here, we assume that when high resolution hyperspectral image is known, the low resolution hyperspectral and high resolution multispectral images are statically independent. We have that $\mathrm{P}(X,Y|Z) = \mathrm{P}(X|Z) \times \mathrm{P}(Y|Z)$. Equation (9) can be rewritten as

$$\mathrm{P}(Z|X,Y) = \frac{\mathrm{P}(X|Z)\mathrm{P}(Y|Z)\mathrm{P}(Z)}{\mathrm{P}(X,Y)} \tag{10}$$

Finally, we note that $\mathrm{P}(X,Y)$ are not functions of Z, and equivalent expression for the MAP equation is given by

$$\hat{Z} = \arg\ \max_Z \mathrm{P}(X|Z)\mathrm{P}(Y|Z)\mathrm{P}(Z) \tag{11}$$

We observe that $\mathrm{P}(X|Z)$ describes the relationship in the first part of the observation model, $\mathrm{P}(Y|Z)$ describes the second part of the observation model, and the third and fourth parts of the observation model is in $\mathrm{P}(Z)$.

The digital number vectors of the multispectral image from different pixels can be assumed to be statistically independent when the high resolution hyperspectral image is given. As a result, when the noise vectors is normally distributed with zero mean and covariance matrix $\mathbf{C_1}$, the conditional probability can be written as

$$\mathrm{P}(X|Z) = \prod_{i\in H} \mathrm{P}(\mathbf{x}_i|\mathbf{z}_i)$$
$$= \prod_{i\in H} \frac{1}{\sqrt{(2\pi)^Q|C_1|}} \exp\{-\frac{1}{2}((\mathbf{x}_i - \boldsymbol{\mu}) - \mathbf{A}\mathbf{z}_i)^{\mathrm{T}}\mathbf{C_1^{-1}}((\mathbf{x}_i - \boldsymbol{\mu}) - \mathbf{A}\mathbf{z}i)\} \quad (12)$$

where H is the set of all pixels in high resolution images. Again, for a given high resolution hyperspectral image, the digital number vectors of different pixels in the low resolution hyperspectral image is assumed to be statistically independent. Furthermore, if the measurement noise is assumed to be Gaussian and pixel and band independent, we have

$$\mathrm{P}(Y|Z) = \prod_{j\in L} \mathrm{P}(\mathbf{y}_j|\mathbf{z}_i)$$
$$= \prod_{j\in L} \frac{1}{\sqrt{(2\pi)^P|C_2|}} \exp\{-\frac{1}{2}\left(\mathbf{y}_j - \frac{1}{K}\sum_{i\in S_j}\mathbf{z}_i\right)^{\mathrm{T}}\mathbf{C_2^{-1}}\left(\mathbf{y}_j - \frac{1}{K}\sum_{i\in S_j}\mathbf{z}_i\right)\} \quad (13)$$

where L is the set of all pixels in low resolution images, and $\mathbf{C_2}$ is a diagonal matrix. It is obvious that the measurement noise cannot be directly observed. As a result, we must estimate it from the experiment.

The conditional PDF of the digital number of a pixel in the high resolution image is a given by

$$\mathrm{P}(Z) = \prod_{i\in H} \mathrm{P}(\mathbf{z}_i)$$
$$= \prod_{i\in H} F\exp\{-\frac{1}{2c_3}\mathbf{z}_i{}^{\mathrm{T}}\mathbf{B}\mathbf{z}_i - \frac{1}{2c_4}\sum_{k\in N_i}\rho_{\mathrm{T}}(\mathbf{z}_i - \mathbf{z}_k)^{\mathrm{T}}\boldsymbol{\Gamma}\,\rho_{\mathrm{T}}(\mathbf{z}_i - \mathbf{z}k)\} \quad (14)$$

where F is a scaled value for normalization and c_3 is a scaled value and can be observed by variance of different digital number between band and neighbor band of each pixel, and c_4 is a scaled value but cannot be observed directly. Thus we must

define it from our experiment. Here, N_i is a neighboring pixel of i, and $\mathbf{\Gamma}$ is diagonal matrix whose elements are 1.

To maximize the expression in (11), we can alternatively minimize the sum of the exponential terms in (12), (13), and (14). Thus, the MAP estimator can be expressed as

$$\hat{Z} = \arg\min_Z \mathrm{C}(Z) \tag{15}$$

where C*(Z)* is defined as

$$\mathrm{C}(Z) = \sum_{j=1}^{M}\left[\frac{1}{2}\left(\mathbf{y}_j - \frac{1}{K}\sum_{i\in S_j}\mathbf{z}_i\right)^{\mathrm{T}}\mathbf{C}_2^{-1}\left(\mathbf{y}_j - \frac{1}{K}\sum_{i\in S_j}\mathbf{z}_i\right)\right] + \sum_{i=1}^{N}\left[\frac{1}{2}((\mathbf{x}_i - \boldsymbol{\mu}) - \mathbf{A}\mathbf{z}i\mathrm{T}\mathbf{C}1{-}1(\mathbf{x}i{-}\boldsymbol{\mu}){-}\mathbf{A}\mathbf{z}i + 12c3\mathbf{z}i\mathrm{T}\mathbf{B}\mathbf{z}i + 12c4k{\in}Ni\rho\mathrm{T}\mathbf{z}i{-}\mathbf{z}k\mathrm{T}\mathbf{\Gamma}\rho\mathrm{T}(\mathbf{z}i{-}\mathbf{z}k)\right. \tag{16}$$

where $\mathrm{C}(\mathbf{z}_i)$ represents $\mathrm{C}(Z)$ at each spatial position *i*, for *i = 1,2,…,N.* Then, the following expression is obtained:

$$\mathrm{C}(\mathbf{z}_i) = \frac{1}{2}((\mathbf{x}_i - \boldsymbol{\mu}) - \mathbf{A}\mathbf{z}_i)^{\mathrm{T}}\mathbf{C}_1^{-1}((\mathbf{x}_i - \boldsymbol{\mu}) - \mathbf{A}\mathbf{z}_i) + \frac{1}{2}\left(\mathbf{y}_j - \frac{1}{K}\sum_{l\in S_j,\, l\neq i}\mathbf{z}_l - \frac{1}{K}\mathbf{z}_i\right)^{\mathrm{T}}\mathbf{C}_2^{-1}\left(\mathbf{x}_i - \frac{1}{K}\sum_{l\in S_j,\, l\neq i}\mathbf{z}_l - \frac{1}{K}\mathbf{z}_i\right) + \frac{1}{2}C_3^{-1}\mathbf{z}_i{}^{\mathrm{T}}B\mathbf{z}_i + \frac{1}{2}C_4^{-1}\sum_{k\in N_i}\rho_{\mathrm{T}}(\mathbf{z}_i - \mathbf{z}_k)^{\mathrm{T}}\mathbf{\Gamma}\rho_{\mathrm{T}}(\mathbf{z}_i - \mathbf{z}_k) \tag{17}$$

It can be shown by us that the optimum solution of (17) can be obtained by iteratively determining the best possible $\mathbf{z}_i$ one pixel a time while data from other pixels are kept as a constant. Furthermore, the closed form solution even for a pixel cannot be directly obtained because fourth term is a non-quadratic function (First, second and third are quadratic functions). Thus we can solve it by using majorization (Stoica and Selén, 2004). Majorization is a commonly used iterative technique where a function is minimized through the minimization of its majorizing function. When we use majorization for fourth term, it can make fourth term to be a quadratic function. We can write

$$C(\mathbf{z}_i) = \frac{1}{2}((\mathbf{x}_i - \boldsymbol{\mu}) - \mathbf{A}\mathbf{z}_i)^{\mathrm{T}}\mathbf{C}_1^{-1}((\mathbf{x}_i - \boldsymbol{\mu}) - \mathbf{A}\mathbf{z}_i) + \frac{1}{2}\left(\mathbf{y}_j - \frac{1}{K}\sum_{l\in S_j,\, l\neq i}\mathbf{z}_l - \frac{1}{K}\mathbf{z}_i\right)^{\mathrm{T}}\mathbf{C}_2^{-1}\left(\mathbf{y}_j - \frac{1}{K}\sum_{l\in S_j,\, l\neq i}\mathbf{z}_l - \frac{1}{K}\mathbf{z}_i\right) + \frac{1}{2}C_3^{-1}\mathbf{z}_i{}^{\mathrm{T}}\mathbf{B}\mathbf{z}_i + \frac{1}{2}C_4^{-1}\sum_{k\in N_i}(\mathbf{z}_i - \mathbf{z}_k)^{\mathrm{T}}\boldsymbol{\Gamma}^{\mathbf{0}}(\mathbf{z}_i - \mathbf{z}_k) \quad (18)$$

where $\boldsymbol{\Gamma}^{\mathbf{0}}$ is diagonal matrix whose elements are 1 for $|\mathbf{z}_{i,b} - \mathbf{z}_{k,b}| \leq T$ or $T/|\mathbf{z}_{i,b} - \mathbf{z}k,b$ for $\mathbf{z}i,b - \mathbf{z}k,b > T$.

Setting the gradient to zero and solving for $\mathbf{z}_i$

$$\widehat{\mathbf{z}_i} = (\mathbf{A}^{\mathrm{T}}\mathbf{C}_1^{-1}\mathbf{A} + \frac{1}{K^2}\mathbf{C}_2^{-1} + C_3^{-1}\mathbf{B} + C_4^{-1}\boldsymbol{\Gamma}^{\mathbf{0}})^{-1}(\mathbf{A}^{\mathrm{T}}\mathbf{C}_1^{-1}(\mathbf{x}_i - \boldsymbol{\mu}) + \frac{1}{K}\mathbf{C}_2^{-1}\mathbf{y}_j - \frac{1}{K}\mathbf{C}_2^{-1}\sum_{l\in S_j,\, l\neq i}\mathbf{z}_l + C_4^{-1}\sum_{k\in N_i}\boldsymbol{\Gamma}^{\mathbf{0}}\mathbf{z}_k) \quad (19)$$

4. Implementation.

First, the low-resolution hyperspectral image is upsampled to have the same size as the high-resolution hyperspectral image. This upsampled image is used as the initial high-resolution hyperspectral image.

Next step, the first pixel of high-resolution hyperspectral image is visited (i =1). Here, the i-th pixel of high-resolution hyperspectral image ($\mathbf{z}_i$) is estimated by solving Equation 19. Then next pixel ($i = i + 1$) is visited to perform the estimation process. The process is continued until the last pixel of hyperspectral image ($i = n$) is visited.

After one update (all pixels are visited and updated), the algorithm computes the total number of changed pixels in Z that has different digital number. If the total number of changed pixels is greater than a predefined threshold, the algorithm returns to the update step in the previous paragraph with the current Z as the initial image, otherwise the algorithm stops and the high-resolution hyperspectral image is obtained. The process described in this section is summarized in the flow chat shown in Figure 15.

Flowchart

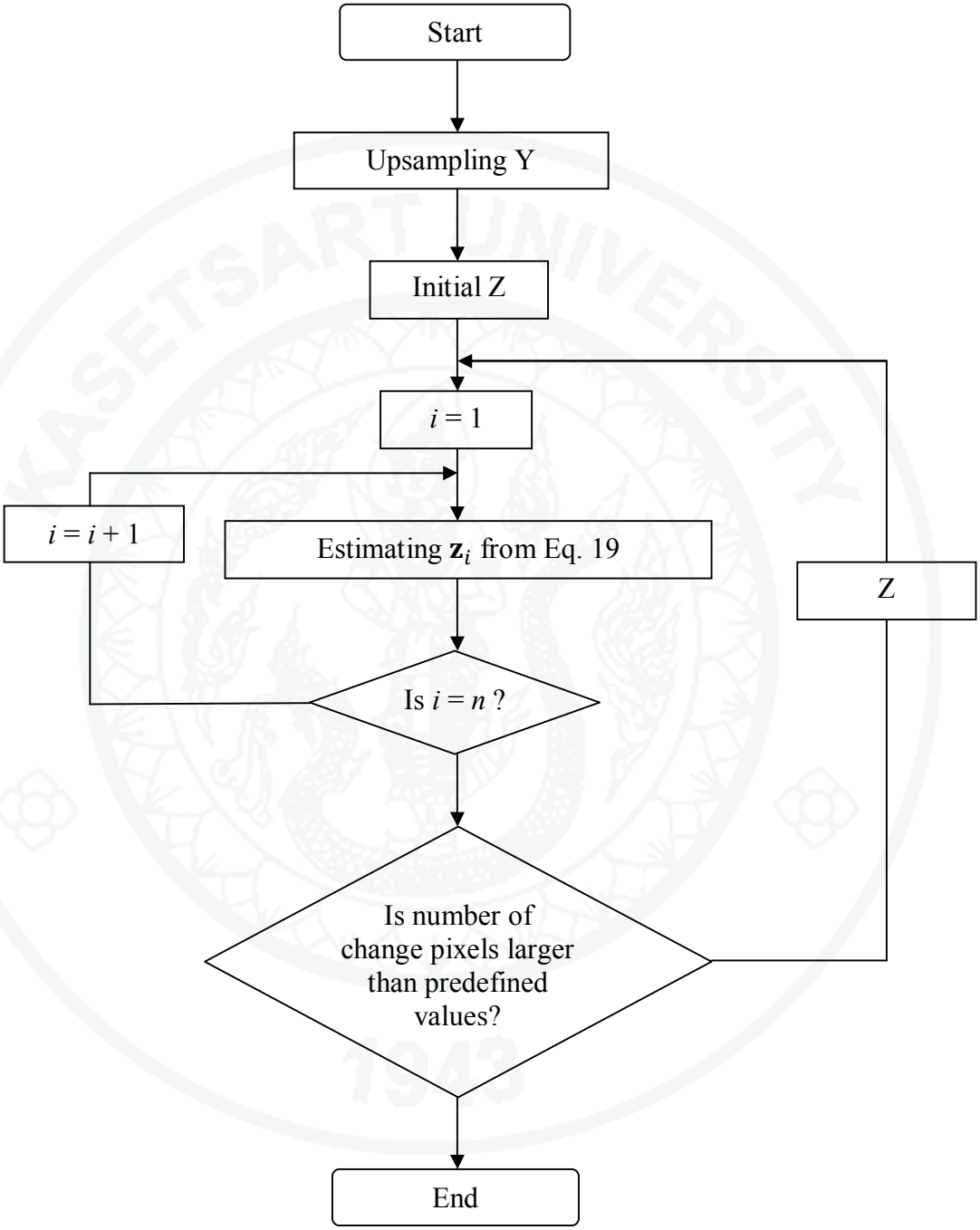

Figure 15 Implementation step

RESULTS AND DISCUSSION

In this thesis, the experiment is divided into two experiments 1) simulation experiment for evaluate performance and 2) fusing of two real images.

Experiment 1

In simulation experiment, to evaluate and compare the fusion performances objectively and quantitatively. Here, we use original hyperspectral image with 115 bands and 300x300 pixels and multispectral image with 4 bands of size 1000x1000 pixels for the first experiment. The original hyperspectral image is use as the reference image with 115 bands and 300x300 pixels (Figure 1). However the original hyperspectral image with 115 bands and 300x300 pixels is spatially smoothed to simulate the low-resolution hyperspectral image with 115 bands and 100x100 pixels (Figure 16) and the original multispectral image with 4 bands and 1000x1000 pixels is spatially smoothed to simulate the high-resolution multispectral image with 4 bands and 300x300 pixels (Figure 17). The resulting fusing hyperspctral image with 115 bands and 300x300 pixels is shown in Figure 18.

From equation (19) solving for $\mathbf{z}_i$, where $\mathbf{A}$ and $\boldsymbol{\mu}$ can be directly observed and estimated by least mean square of the relationship between high-resolution hyperspectral image and multispectral image (equation in (4)). The values of $\mathbf{A}$ and $\boldsymbol{\mu}$ are shown in Appendix. And $\mathbf{C_1}$ can be directly observed and estimated covariance error of the relationship between high-resolution hyperspectral image and multispectral image. The values of $\mathbf{C_1}$ is shown in Appendix. And $\mathbf{C_2}$ cannot be directly observed and we must define it from our experiment. The best values of $\mathbf{C_2}$ is diagonal matrix size of 115x115 whose elements are 1. And c_3 can be directly observed and estimated by variance of different digital number between band and neighbor band (equation in (6)). The value of c_3 is 10.9465. And c_4 cannot be directly observed and we must define it from our experiment. The best value of c_4 is 10000. Finally, T for $\boldsymbol{\Gamma^0}$ size of 115x115 cannot be directly observed and we must define it from our experiment. The best value of T is 25.

Since hyperspectral and multispectral images have over bands to show in true color model. So we choose three bands which are interesting and necessary to show in false color model. The bands are chosen by us to show in false color model that are Blue: 20th band, Green: 50th band, and Red: 100th band for hyperspectral image and Blue: 1st band; Green: 2nd band; and Red: 4th band for multispectral image.

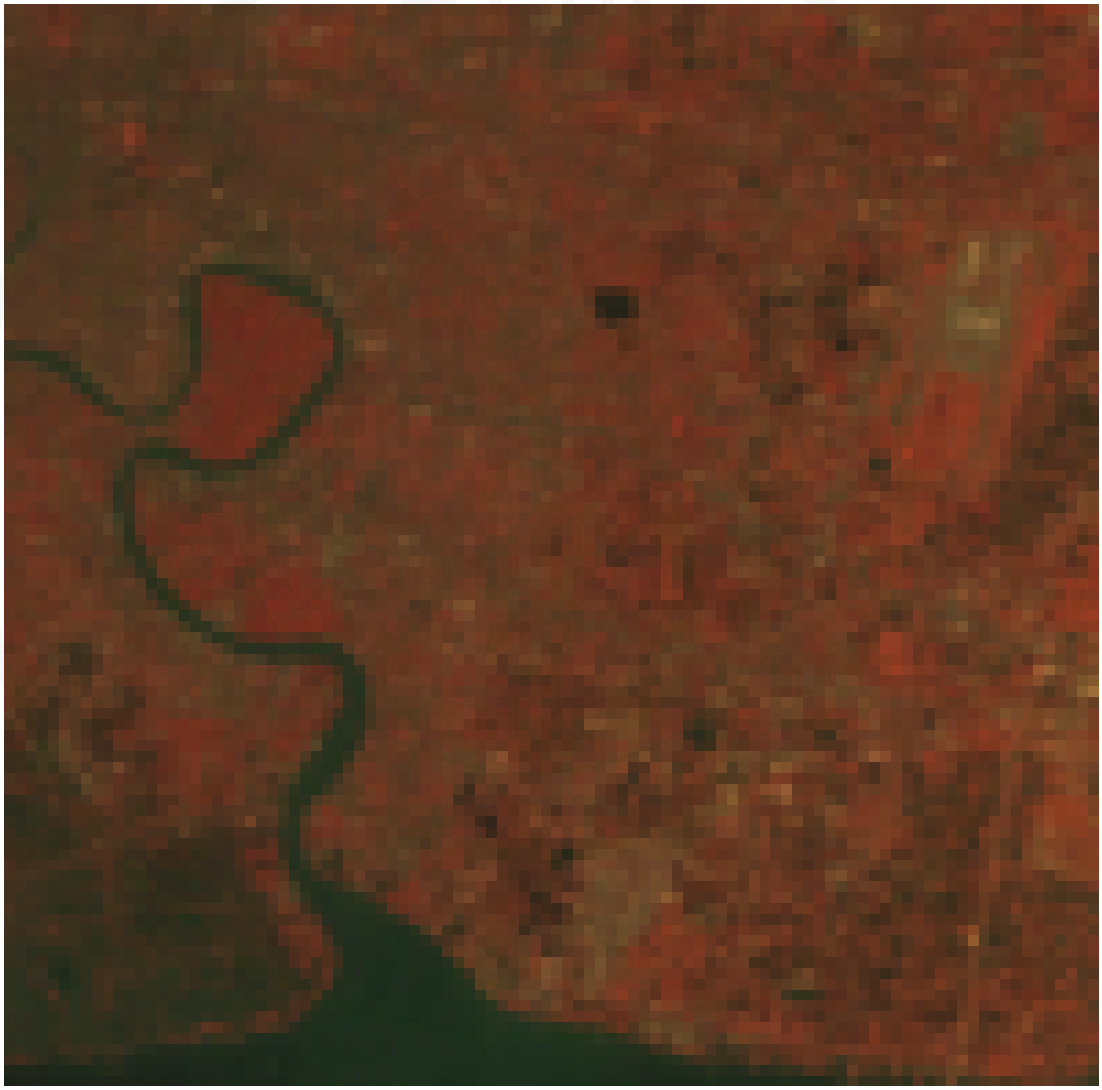

Figure 16 Low-resolution hyerspectral image (degraded image) (100x100 pixels, 115 bands)

Figure 17 High-resolution multispectral image (degraded image) (300x300 pixels, 4 bands)

Figure 18 High-resolution hyperspectral image (fused image) (300x300 pixels, 115 bands)

For quantitatively measures, we use four evaluation metrics 1) the root mean square error (RMSE), 2) the signal to noise ratio (SNR) in decibels (dB), 3) the averaged spectral angle mapper (SAM) (Yuhas, Goetz, and Boardman, 1992), and 4) a universal image quality index (UIQI) (Wang, and Bovik, 2002). The first and second index is a similarity and used to measure for the spatial improvement. If RMSE value is lower and SNR is higher, performance is better. The third index is used to measure for the spectral improvement. If SAM value is lower, performance is better. The last index is used to measure for the spatial and spectral improvement. If UIQI value is closer to one, performance is better.

In the experiment, we compare the performance of our proposed fusion technique with Hardie algorithm for hyperspectral image resolution enhancing using an auxiliary sensor (Hardie et al., 2004). The results are listed in Table 3.

Table 3 Comparison performance

	Hardie algorithm	Proposed
RMSE	3.4620	2.7675
SNR (dB)	59.5450	64.0225
SAM (degree)	1.3757	1.5300
UIQI	0.9471	0.9504

From Table 3, we observe that the significant improvement is obtained. Especially in the spatial improvement, our proposed fusion algorithm performs significantly much better than the Hardie algorithm (RMSE is lower 0.6945 and SNR is higher 4.4775 dB). It seems that Huber-MRF can enhance the spatial resolution effectively. However, in the spectral improvement, our proposed fusion technique is little worse than the Hardie algorithm (SAM is higher 0.1543 degree). When considering the overall performance (UIQI is higher 0.0033) our proposed algorithm still outperforms the Hardie algorithm. To check for the spectral integrity of our fusion algorithm, we examine the spectral responses (Figures 19, 21, and 23) at three homogenous areas, namely, vegetation, building and water and the resulting root mean square errors (RMEs) are 1.81, 1.8902 and 1.3477, respectively. The performance of the Hardie algorithm is also investigated, and the spectral responses are plotted in Figures 20, 22 and 24, for vegetation, building and water, respectively. The RMEs for vegetation, building and water are 2.9676, 2.7524 and 1.3251, respectively. Clearly, our algorithm performs significantly better for classes of vegetation and building whereas the performance is slightly dropped for the class of water since majority of pixels in the image is covered by building and vegetation. Our algorithm is, then, tuned for the majority.

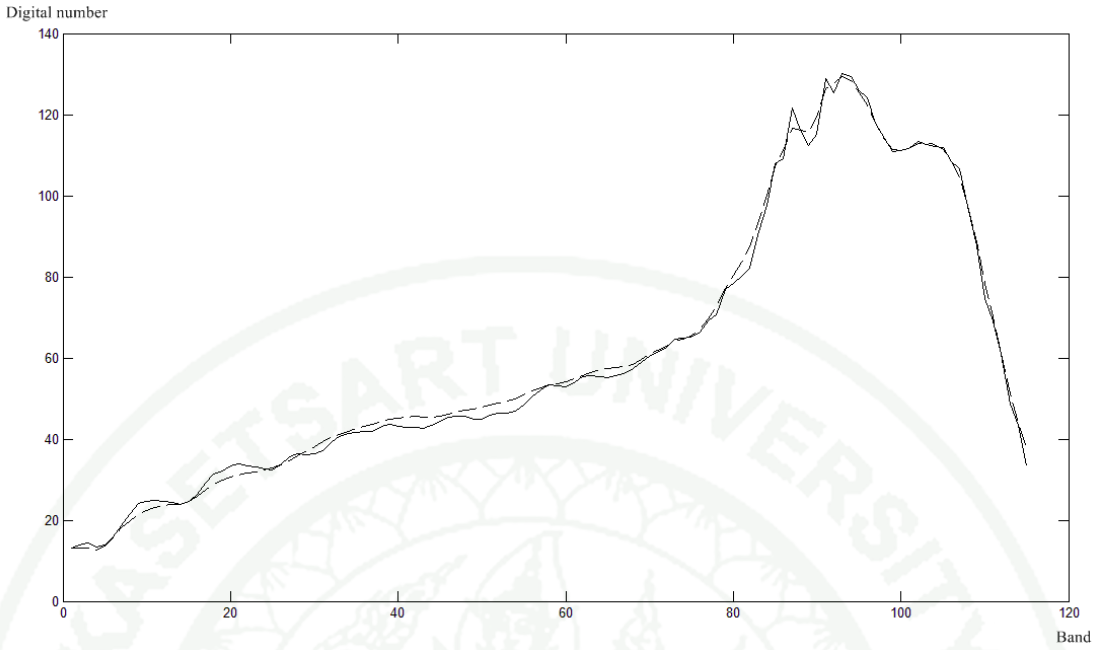

Figure 19 Comparison digital number vector of hyperspectral pixel at pixel (100, 75) on vegetation area between reference pixel (solid line) and proposed fused pixel (dash line) (RMSE is 1.8100)

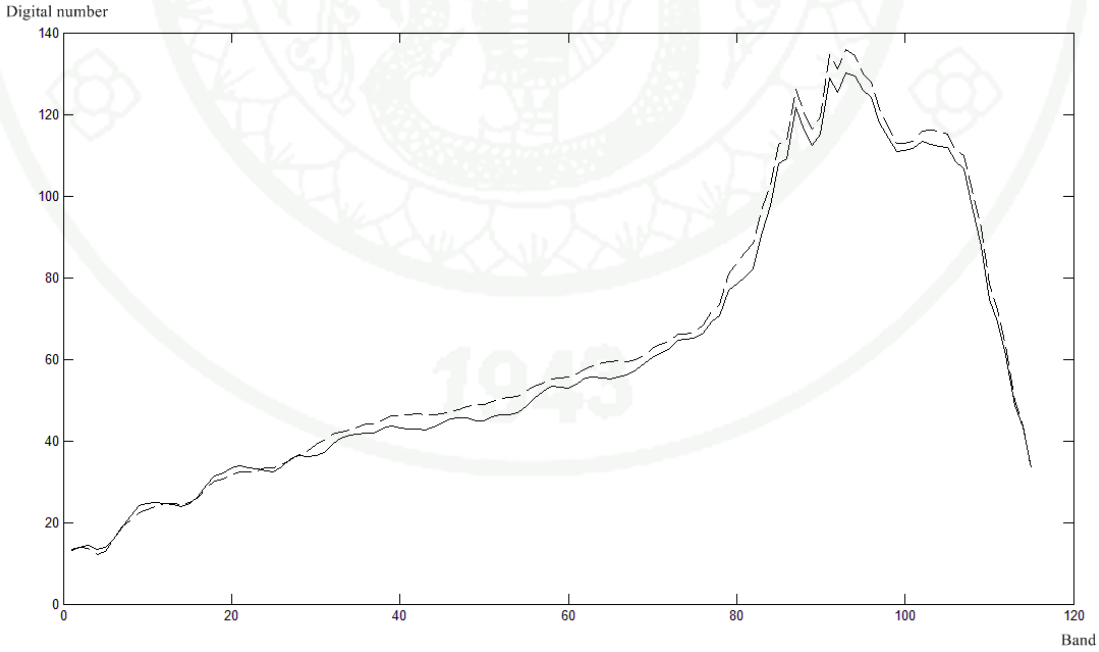

Figure 20 Comparison digital number vector of hyperspectral pixel at pixel (100, 75) on vegetation area between reference pixel (solid line) and Hardie fused pixel (dash line) (RMSE is 2.9697)

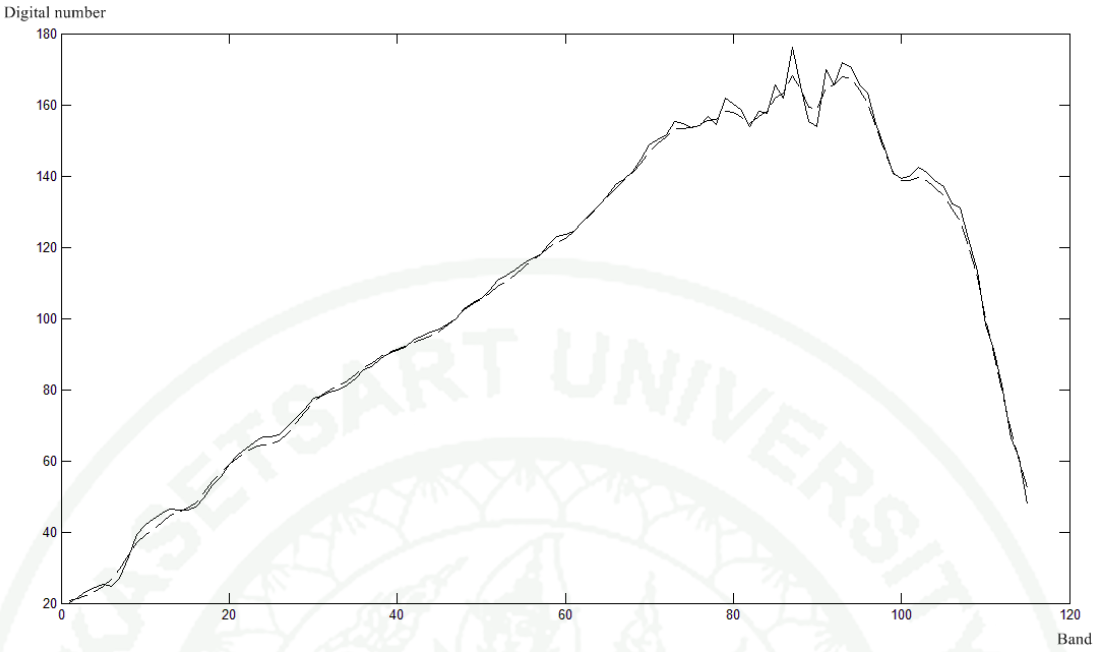

Figure 21 Comparison digital number vector of hyperspectral pixel at pixel (90, 270) on building area between reference pixel (solid line) and proposed fused pixel (dash line) (RMSE is 1.8902)

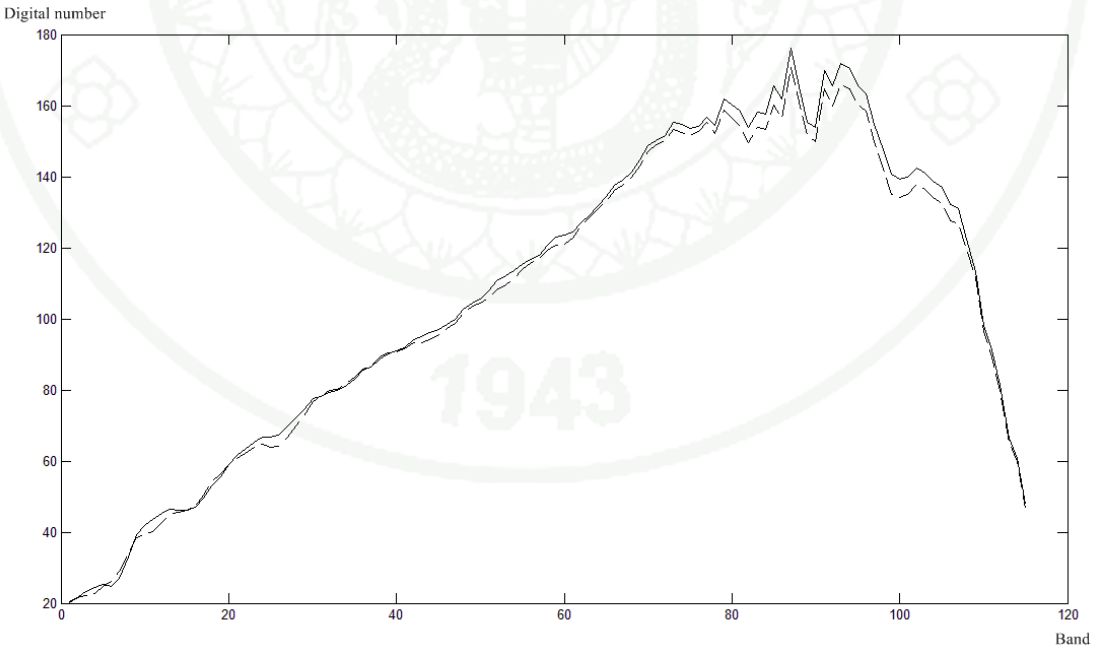

Figure 22 Comparison digital number vector of hyperspectral pixel at pixel (90, 270) on building area between reference pixel (solid line) and Hardie fused pixel (dash line) (RMSE is 2.7524)

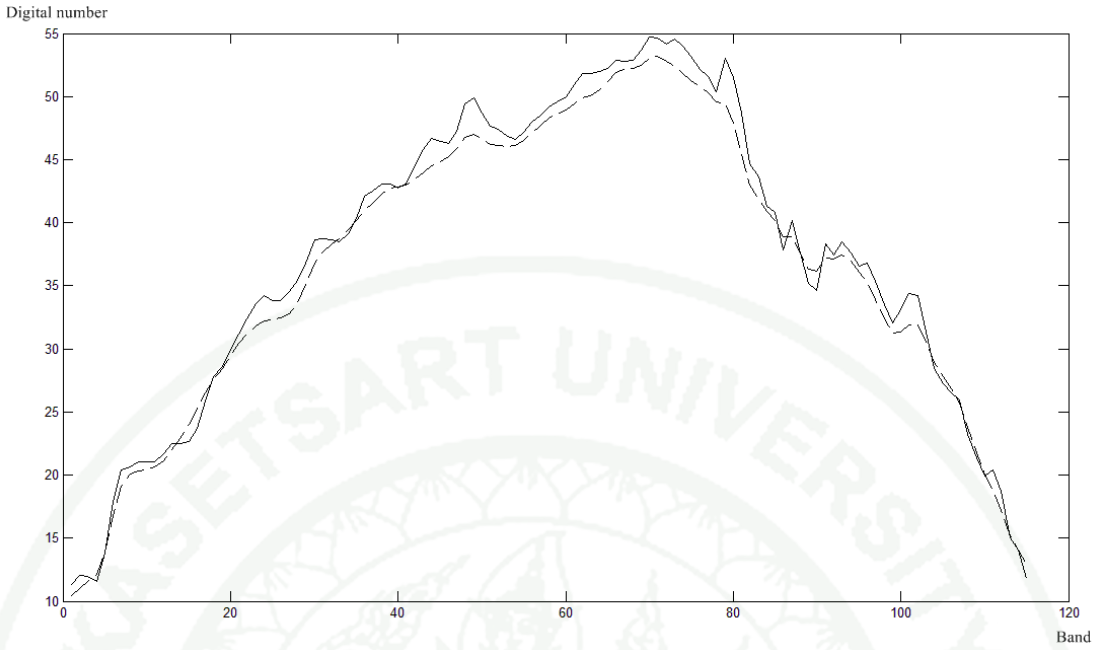

Figure 23 Comparison digital number vector of hyperspectral pixel at pixel (285, 105) on water area between reference pixel (solid line) and proposed fused pixel (dash line) (RMSE is 1.3477)

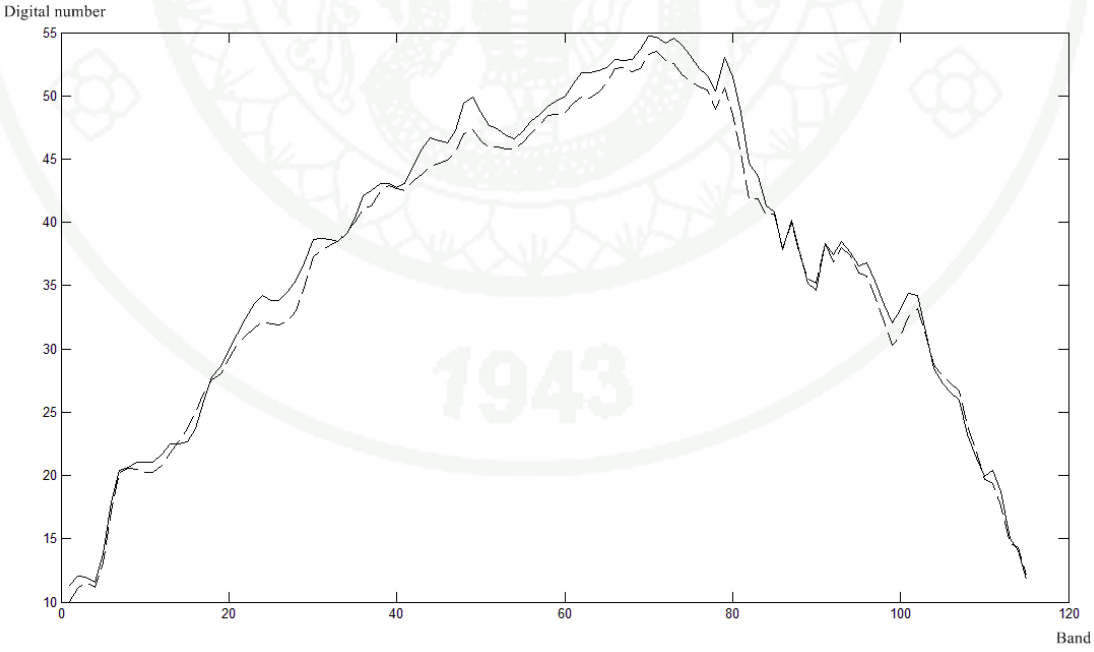

Figure 24 Comparison digital number vector of hyperspectral pixel at pixel (285, 105) on water area between reference pixel (solid line) and Hardie fused pixel (dash line) (RMSE is 1.3251)

Another key performance metrics for image reconstruction is the edge preservation in the fused image. We plotted at digital numbers of the reference data on the 100th bands of Lines 100, 200 and 280 comparing with the fused images from our proposed and Hardie algorithm (Figures 25- 30). The RMES are also computed and the values for the proposed algorithm are 3.0904, 2.977 and 3.6022 whereas the values for the Hardie algorithm are 4.4631, 4.5065 and 5.2546, for Lines 100, 200 and 280, respectively. We further investigate the edge displacement and faults edges of the fused images by applying the derivative operation on the single-line and single-band strips, i.e.,

$$\mathrm{f}'(i) = \mathrm{f}(i) - \mathrm{f}(i+1) \tag{20}$$

where $\mathrm{f}'(i)$ is result of first derivative at pixel i and $\mathrm{f}(i)$ is digital number at pixel i. Next, edges are identified as the point where the magnitude of derivatives is greater than 15. The results are shown in Figures 31-36. Obviously, the Hardie algorithm produces more faults edges than our algorithm for all sets of data.

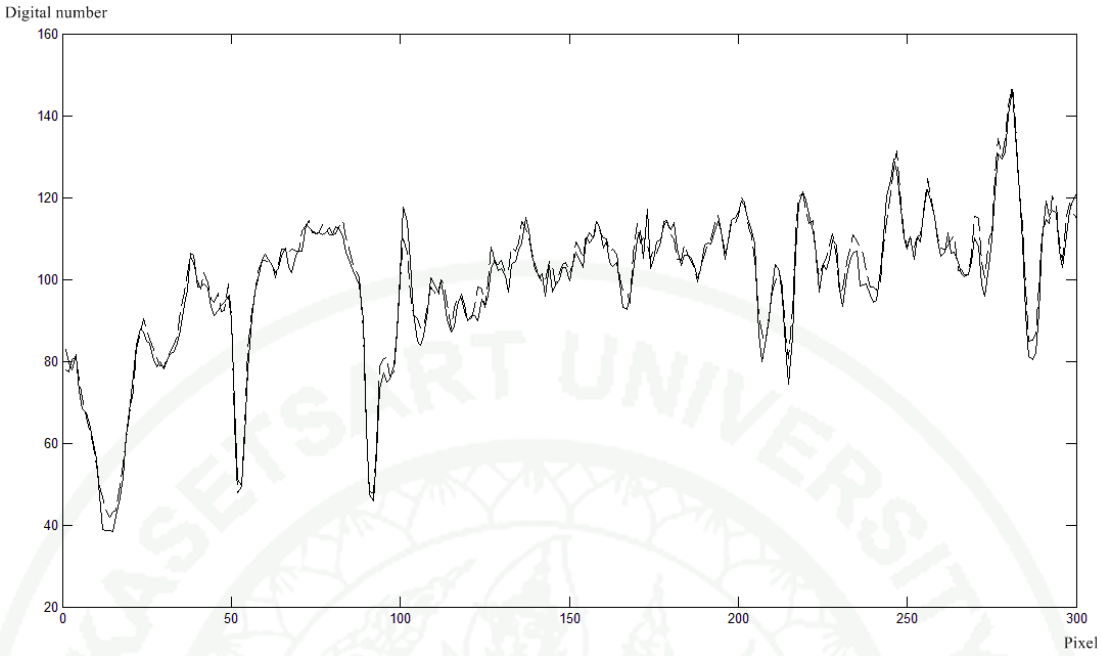

Figure 25 Comparison digital number on line 100 in hyperspectral image at band 100th between reference pixels (solid line) and proposed fused pixels (dash line) (RMSE is 3.0904)

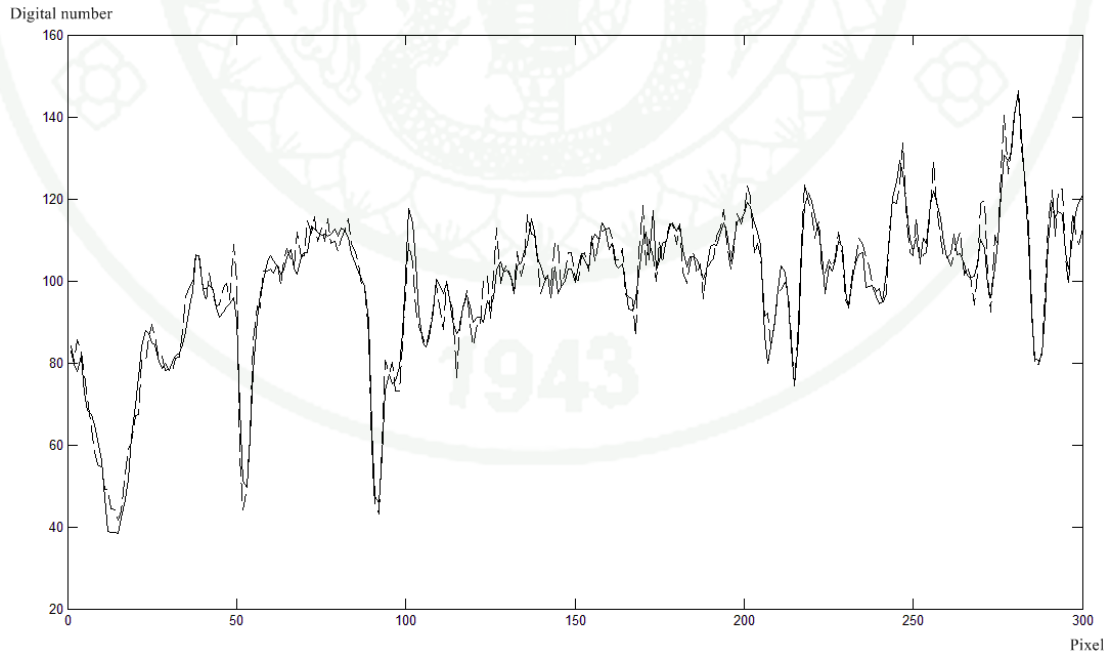

Figure 26 Comparison Digital number on line 100 in hyperspectral image at band 100th between reference pixels (solid line) and Hardie fused pixels (dash line) (RMSE is 4.4631)

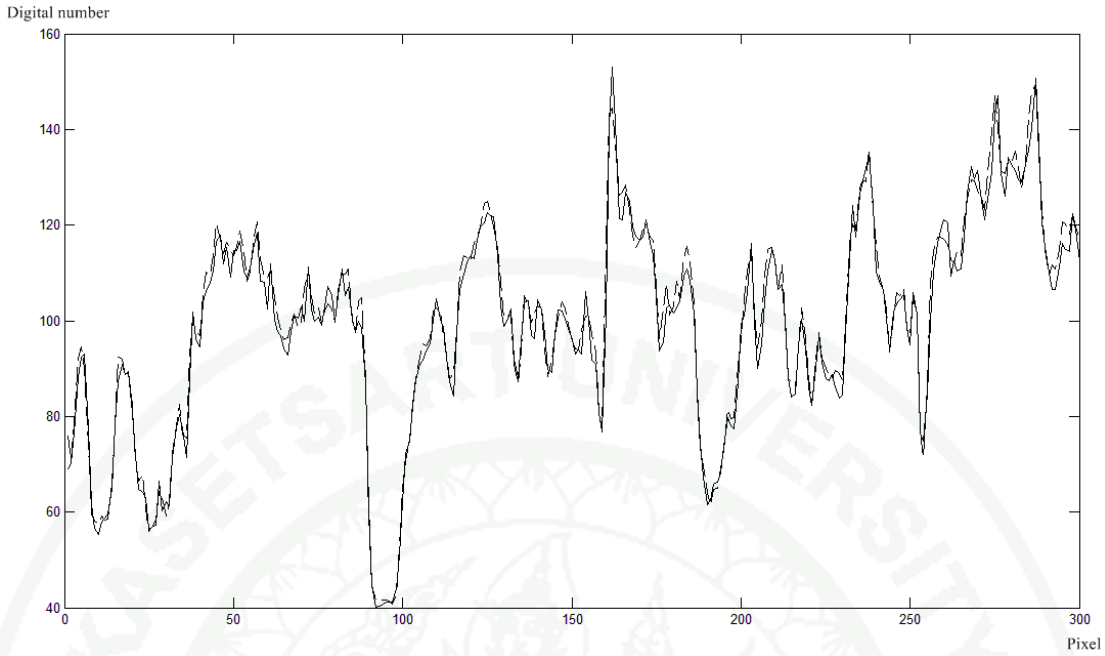

Figure 27 Comparison digital number on line 200 in hyperspectral image at band 100th between reference pixels (solid line) and proposed fused pixels (dash line) (RMSE is 2.9773)

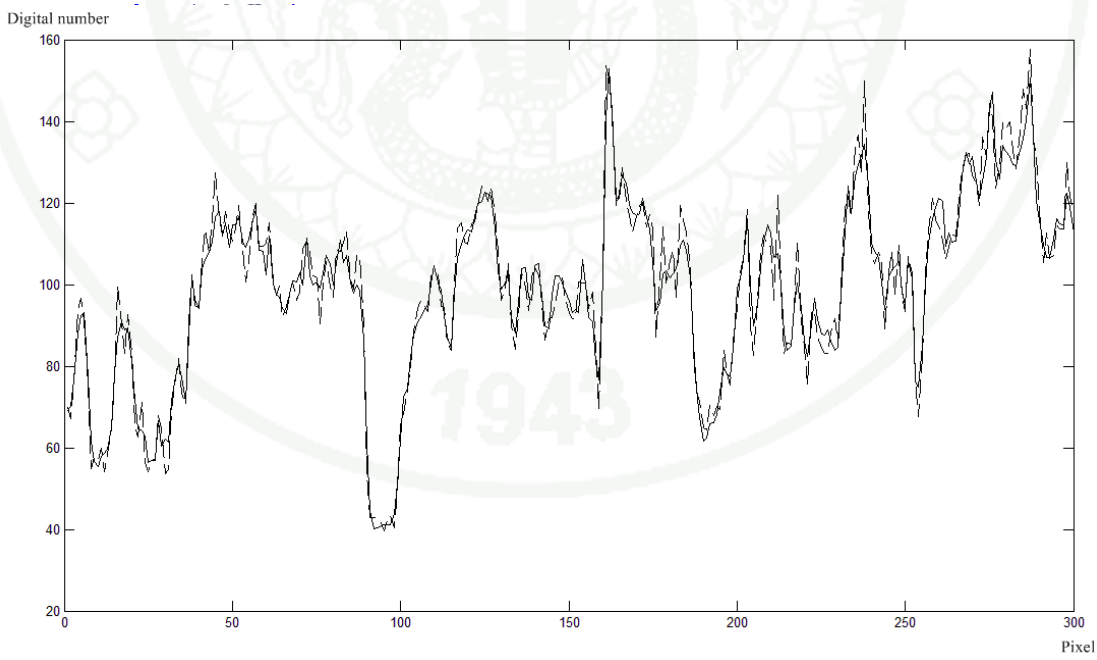

Figure 28 Comparison digital number on line 200 in hyperspectral image at band 100th between reference pixels (solid line) and Hardie fused pixels (dash line) (RMSE is 4.5065)

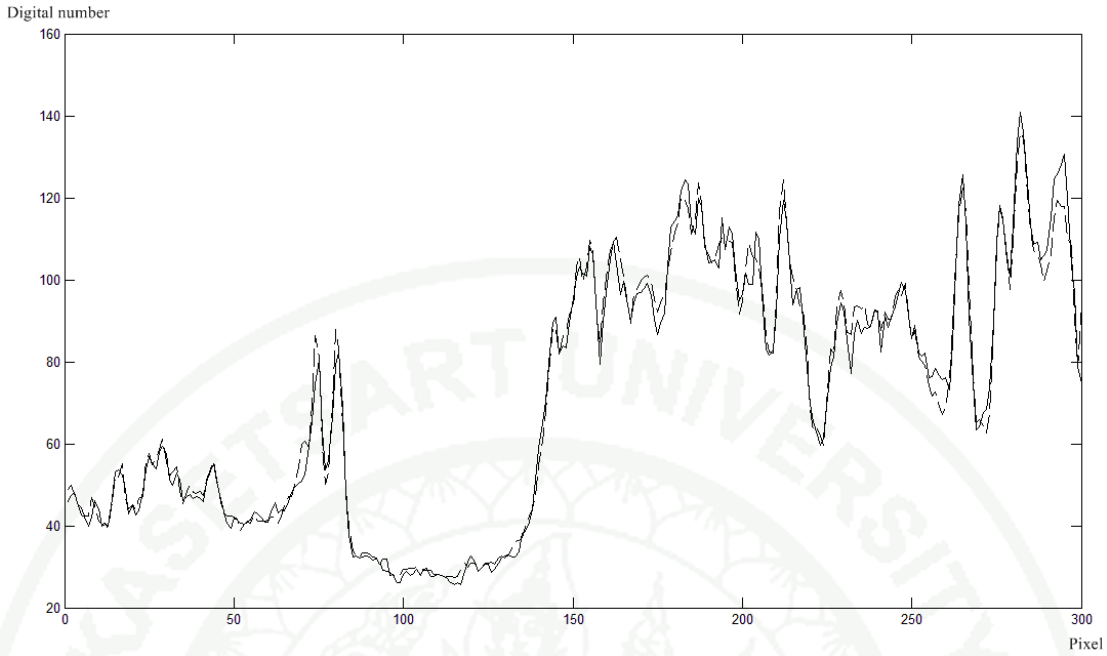

Figure 29 Comparison digital number on line 280 in hyperspectral image at band 100th between reference pixels (solid line) and proposed fused pixels (dash line) (RMSE is 3.6022)

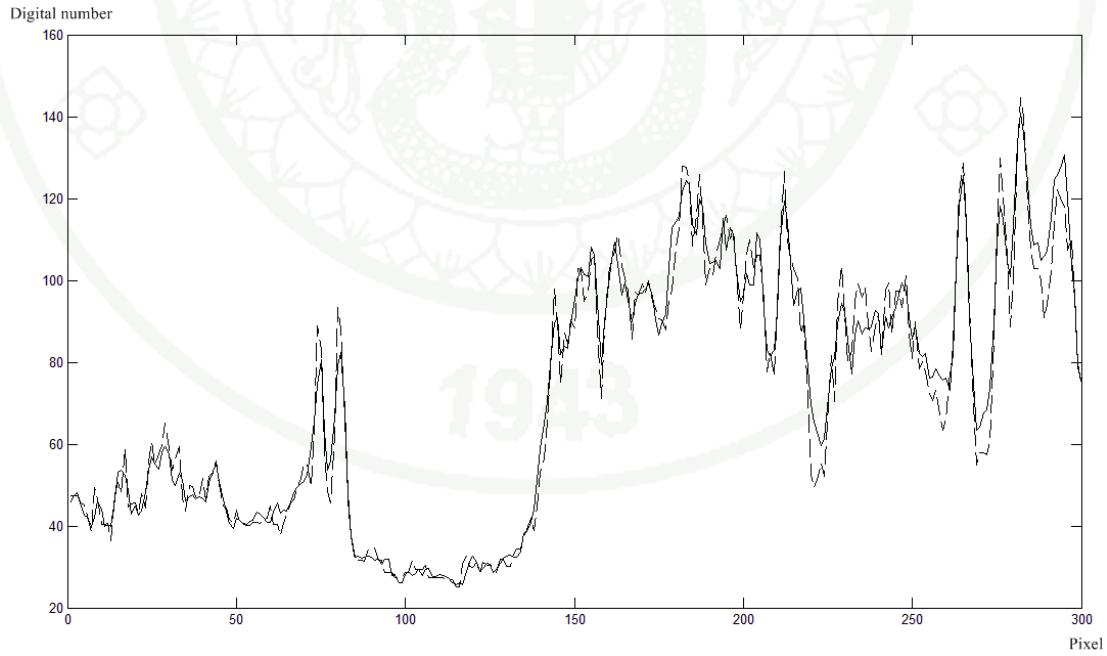

Figure 30 Comparison Digital number on line 280 in hyperspectral image at band 100th between reference pixels (solid line) and Hardie fused pixels (dash line) (RMSE is 5.2546)

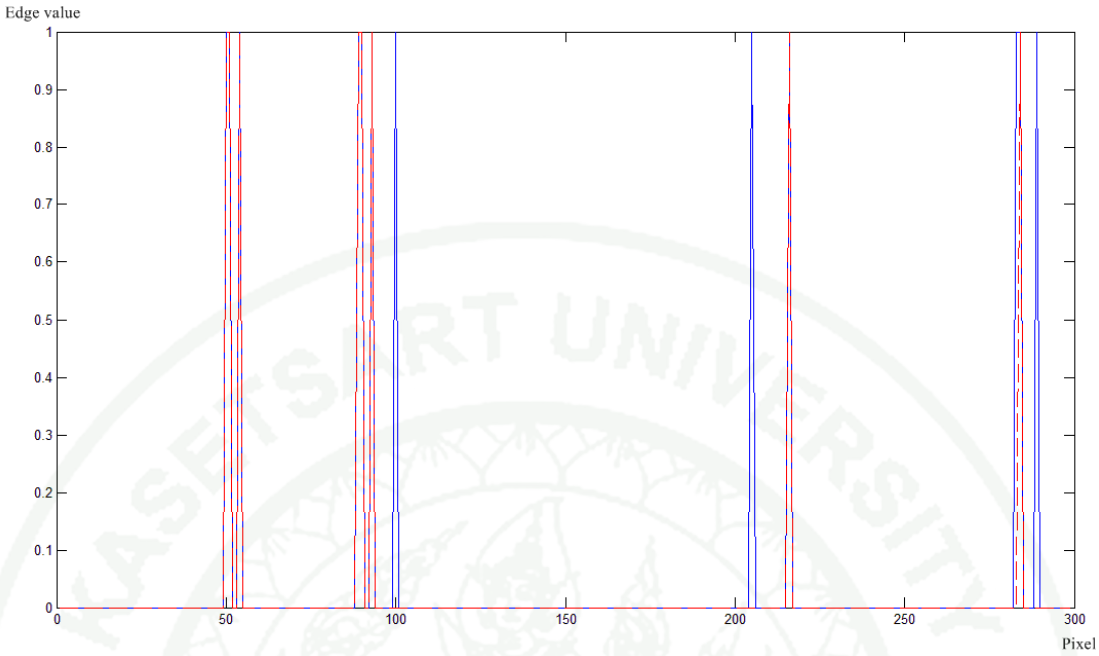

Figure 31 Comparison edge value on line 100 in hyperspectral image at band 100th between reference pixels (blue solid line) and proposed fused pixels (red dash line)

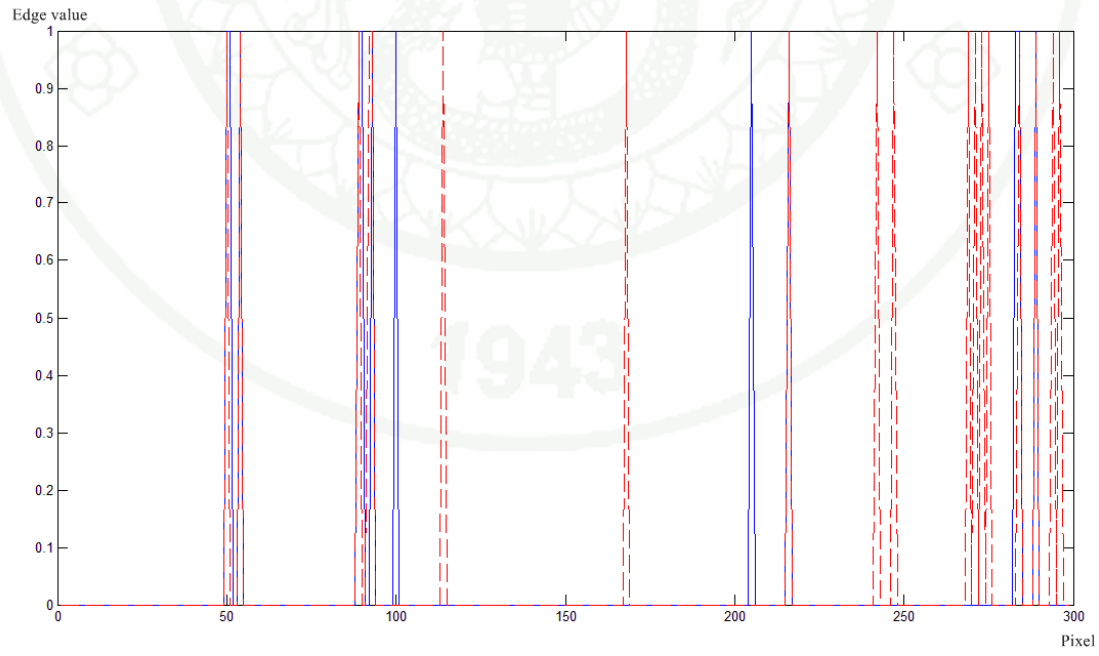

Figure 32 Comparison edge value on line 100 in hyperspectral image at band 100th between reference pixels (blue solid line) and Hardie fused pixels (red dash line)

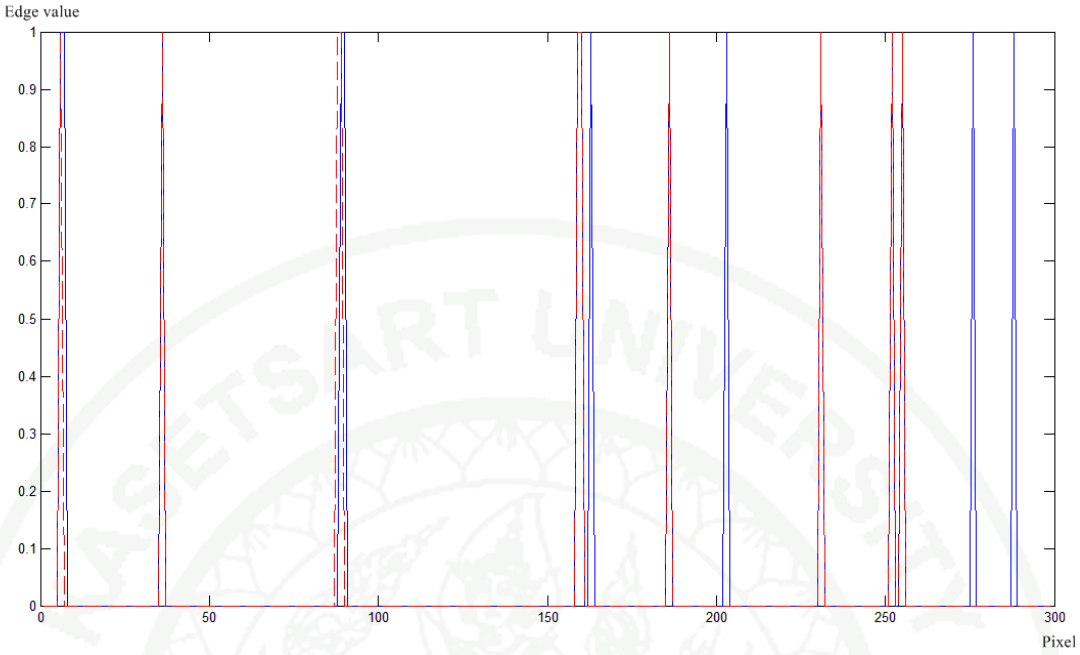

Figure 33 Comparison edge value on line 200 in hyperspectral image at band 100th between reference pixels (blue solid line) and proposed fused pixels (red dash line)

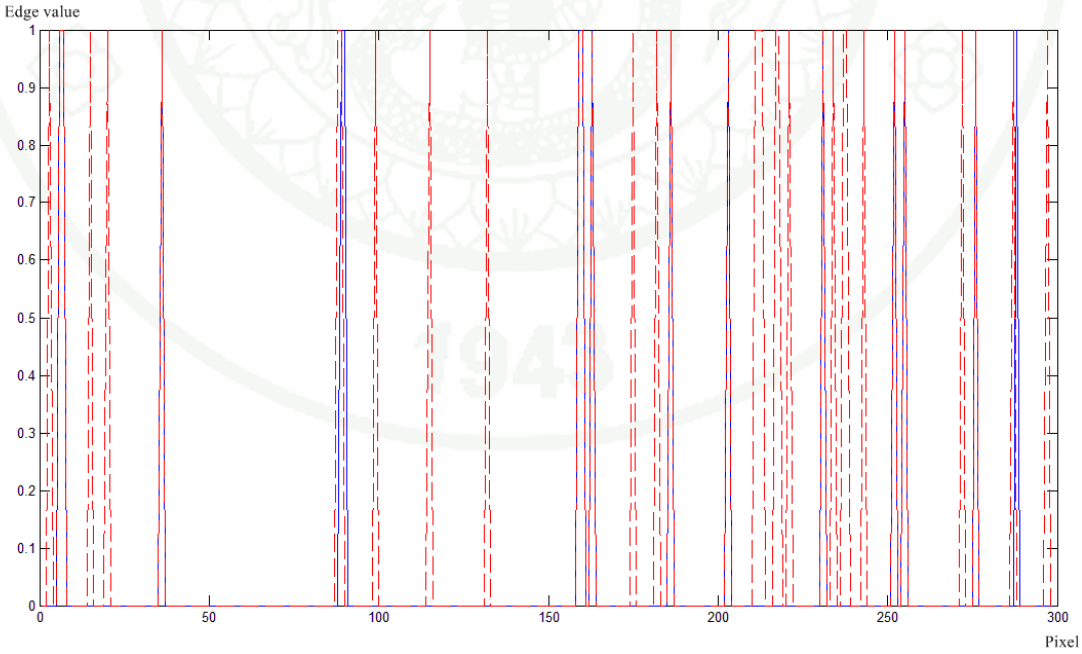

Figure 34 Comparison edge value on line 200 in hyperspectral image at band 100th between reference pixels (blue solid line) and Hardie fused pixels (red dash line)

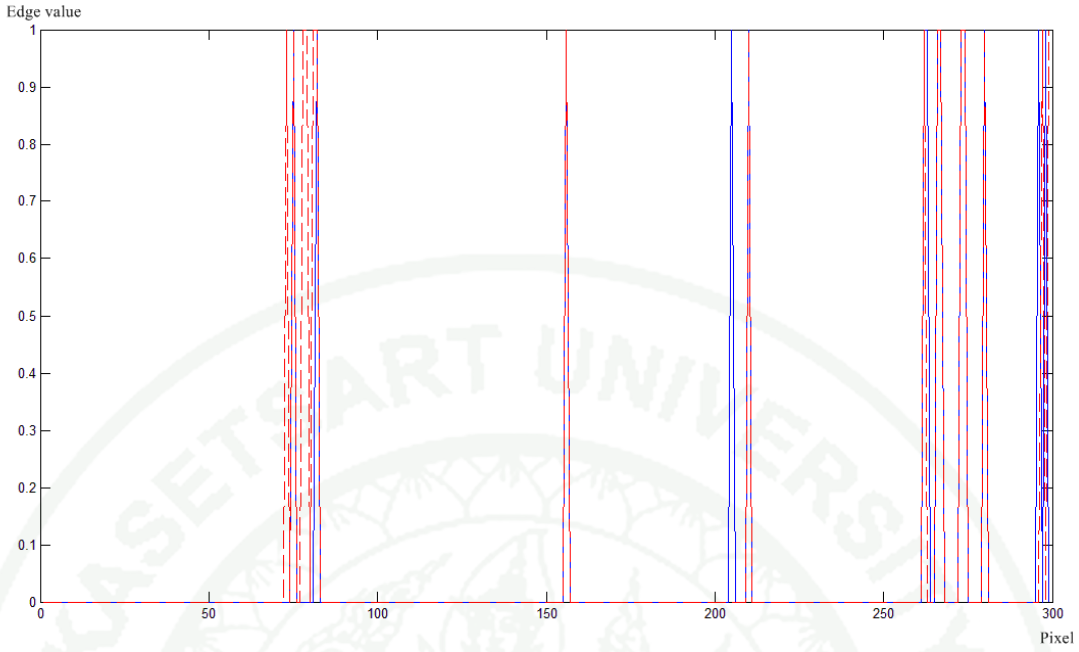

Figure 35 Comparison edge value on line 280 in hyperspectral image at band 100th between reference pixels (blue solid line) and proposed fused pixels (red dash line)

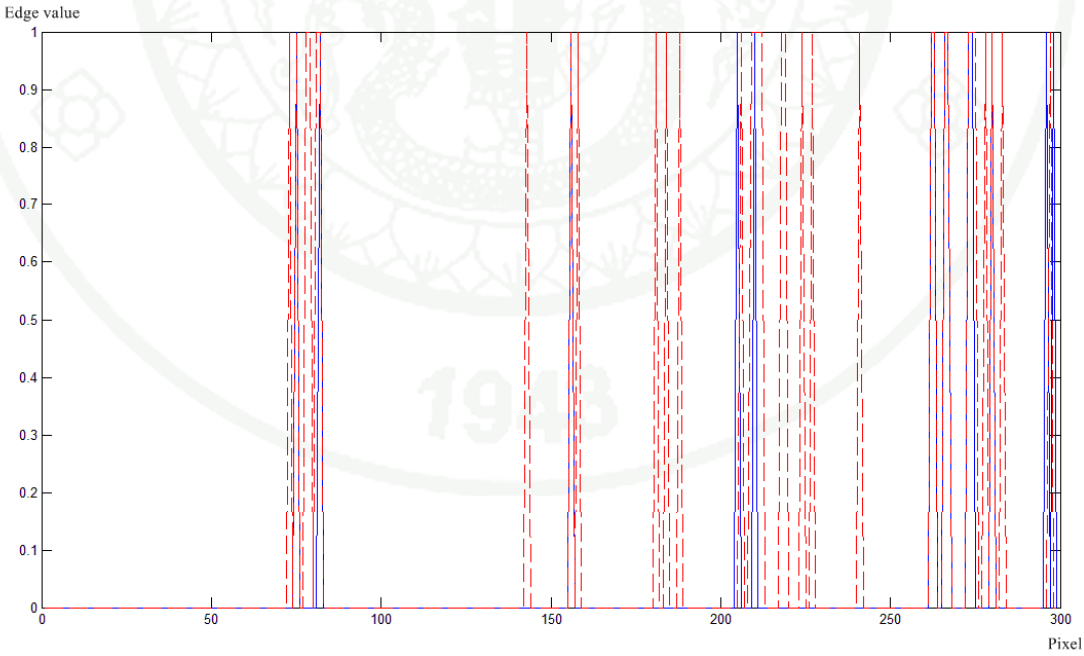

Figure 36 Comparison edge value on line 280 in hyperspectral image at band 100th between reference pixels (blue solid line) and Hardie fused pixels (red dash line)

By observing Figures 37, 38 and 39, it appears that the fused hyperspectral image using the Hardie algorithm appears to be more contrast and sharper than the our proposed fused image (Figure 37) since the algorithm proposed by Hardie does not take the spatial correlation of hyperspectral data into the consideration whereas the proposed algorithm incorporates the correlation into the model. The Hardie fused image looks over contrast and sharp (Figure 38) when compares with reference image (desired image) while the proposed fused image looks more similar to reference image than the Hardie fused image (Figure 39). Again for visualization performance, the proposed algorithm works better for integrating images

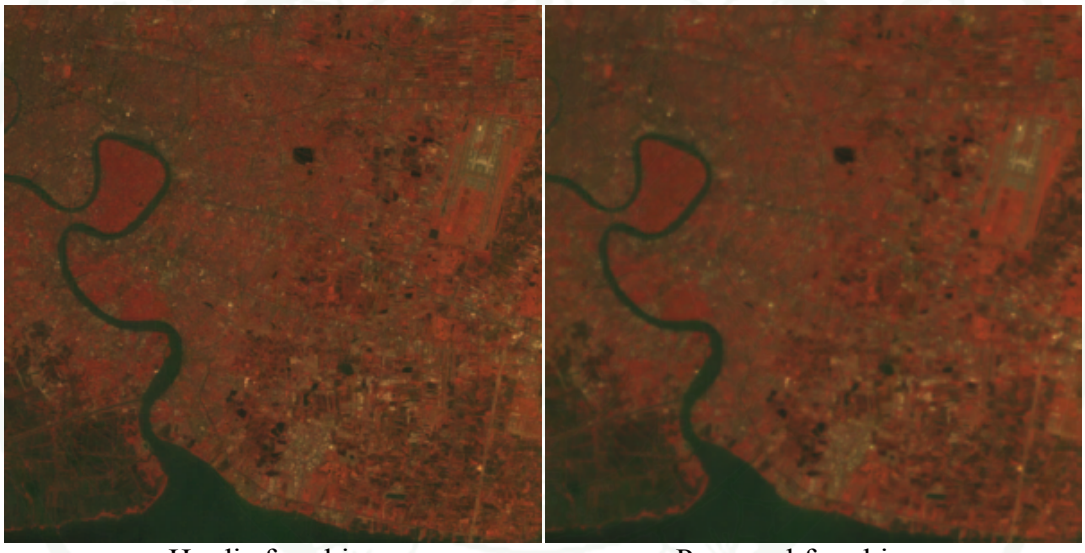

Hardie fused image Proposed fused image

Figure 37 Comparison between Hardie fused and proposed fused images

Hardie fused image Reference image

Figure 38 Comparison between Hardie fused and reference images

Proposed fused image Reference image

Figure 39 Comparison between proposed fused and reference images

Experiment 2

In the fusing of two real images, the proposed fusion technique is used to apply for real work where there is no ground data. Thus, we can evaluate the performance by using visual inspection only. We apply the original hyperspectral image with 115 bands and 300x300 pixels (low-resolution hyperspectral image), shown in Figure 1 and the multispectral image with 4 bands and 900x900 pixels (high-resolution multispectral image) downsampled from the original multispectral image with 4 bands and 1000x1000 pixels, shown in Figure 40 to produce fused hyperspectral image with 115 bands and 900x900 pixels (high-resolution hyperspectral image), shown in Figure 41.

By applying the parameters $\mathbf{A}$, $\boldsymbol{\mu}$, $\mathbf{C_1}$, $\mathbf{C_2}$, c_3, c_4 and T from Experiment 1. The multispectral image is degraded to 900x900 to keep the resolution ratio between high and low resolution images as an integer to expedite the computational process. Our algorithm can be generalized into any ratio of resolutions.

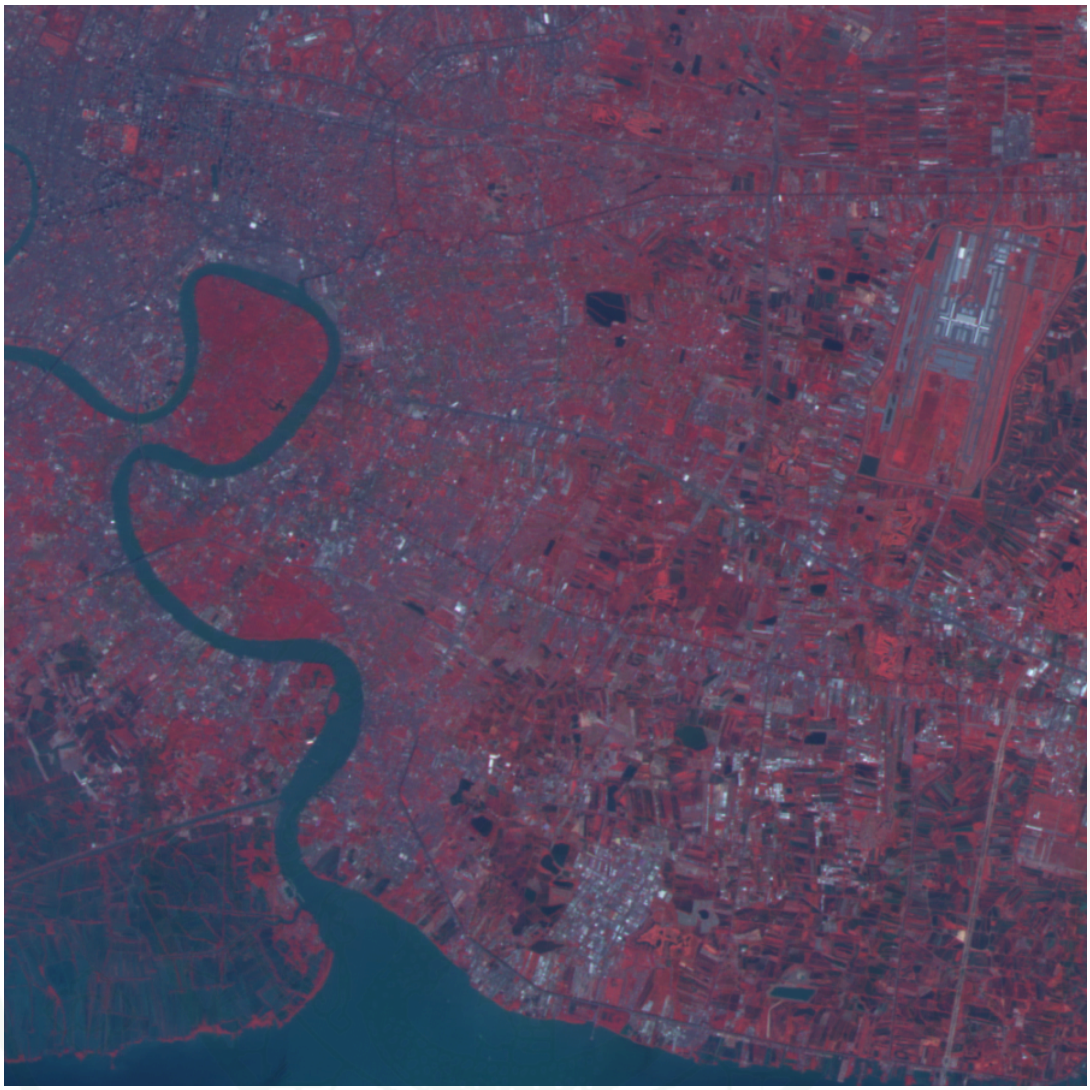

Figure 40 High-resolution multispectral image (900x900 pixels, 4 bands)

Figure 41 High-resolution hyperspectral image (fused image) (900x900 pixels, 115 bands)

Since we do not have the high resolution hyperspectral image for quantitative comparison, we use low-resolution hyperspectral image (original image) as a reference for comparison by visual inspection (Figure 42). In Figure 43, the region of Suvarnabhumi airport is selected for more detail comparison since this area has a lot of fine detail and easy to find on the image. Clearly, our algorithm shows the significant improvement from the original image in term of sharpness and texture. Lastly, we compare our proposed algorithm with the Hardie algorithm in Figure 44. By visual inspection alone, we cannot observe the different between them.

Fused image Original image

Figure 42 Comparison between the fused and original images

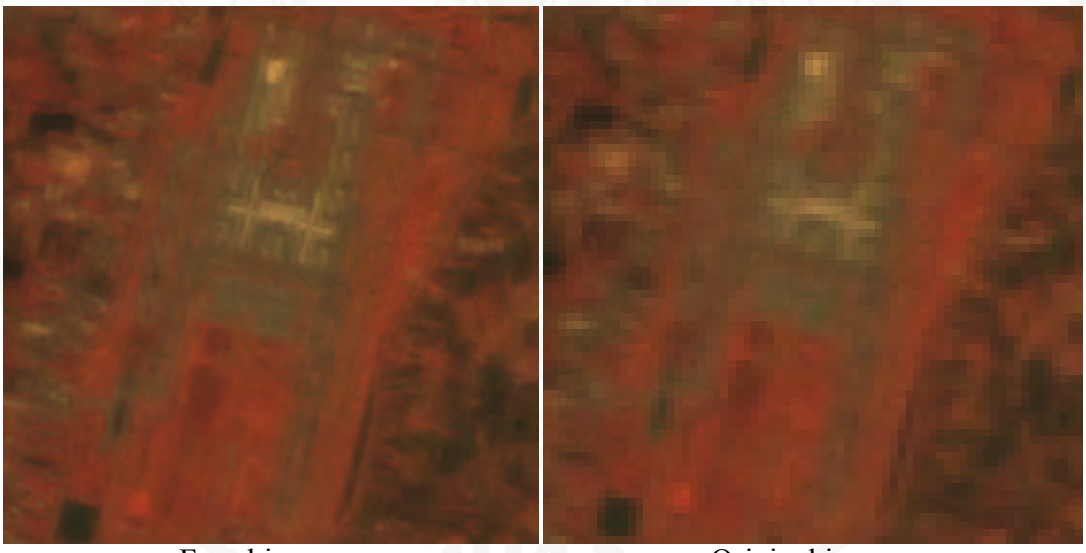

Fused image Original image

Figure 43 Comparison between the fused and original images focused on Suvarnabhumi Airport

Proposed fused image Hardie fused image

Figure 44 Comparison between the proposed fused and Hardie fused images

CONCLUSION AND RECOMMENDATION

Conclusion

In this thesis, we develop the new image fusion for combining hyperspectral and multispectral images. The fusion of hyperspectral and multispectral images is a process that merges high spectral resolution image (low-resolution hyperspectral image) with high spatial resolution image (high-resolution multispectral image) to produce fused image with high spatial and high spectral resolutions (high-resolution hyperspectral image).

We propose fusion of hyperspectral and multispectral image based on statistical model. In the observation model, we divided observation model into four parts; (1) the relationship between high spatial resolution multispectral and hyperspectral images, (2) the relationship between a low-resolution and a high-resolution hyperspectral images, (3) the band to band relationship, (4) the relationship of digital numbers among neighboring pixels. In the estimation strategy, we employ the MAP criteria for estimation from the observation model. A closed-form solution of the fused images is also derived in this thesis.

Experimental results show that the proposed fusion algorithm has efficiency for fusing hyperspectral and multispectral images. In simulation experiment, we compare the performance of our proposed fusion technique with Hardie algorithm for hyperspectral image resolution enhancing using an auxiliary sensor. In the spatial improvement, our proposed fusion technique is much better performance than the Hardie algorithm in terms of RMSE and SNR. However, in the spectral improvement, our proposed fusion technique is little worse than the Hardie algorithm in term of SAM. Both of spatial and spectral improvement, our proposed fusion is still better performance than the Hardie algorithm in term of UIQI. For visualization evaluation, the proposed fused image has more similar to reference image than the Hardie algorithm. In fusing of real image experiment, the proposed fused image is also effective by visualization evaluation.

Recommendation

Since this thesis only examined the performance on one SMMS data scene, we recommend that this proposed algorithm should be performed on more data either from SMMS or other satellites.

Since this thesis is based on the fusion of co-registered hyperspcetral and multispectral images, the further study where hyperspcetral and multispectral image are not perfectly aligned will be next step of future research for the fusion algorithm. In this recommendation, we carries out the preliminary investigation of fusion of mis-registered hyperspectral and multispectral images. Due to the quality of fused images degrades significantly when the multispectral and hyperspectral image are not perfectly registered. So the combining of fusion and registration technique is employed to improve the quality of fused images with misregistered images. Such as a work in (Chen, GUo, Leung, and Bosse, 2010) attempts to jointly fuse and registered two image pair using the expectation maximization algorithm.

Our simple experiment shows that the significant performance improvement over the spatially enhanced hyperspectral image without considering the registration error can obtain when applying our proposed algorithm.

Table 4 Comparison fused image

	x	y	θ	RMSE
fused hyperspectral image without registration error	0	0	0	3.4638
fused hyperspectral image with registration error	2	3	3	5.5131
fused hyperspectral image with registration error using our algorithm	-0.1629	-0.2626	-0.3646	2.7715

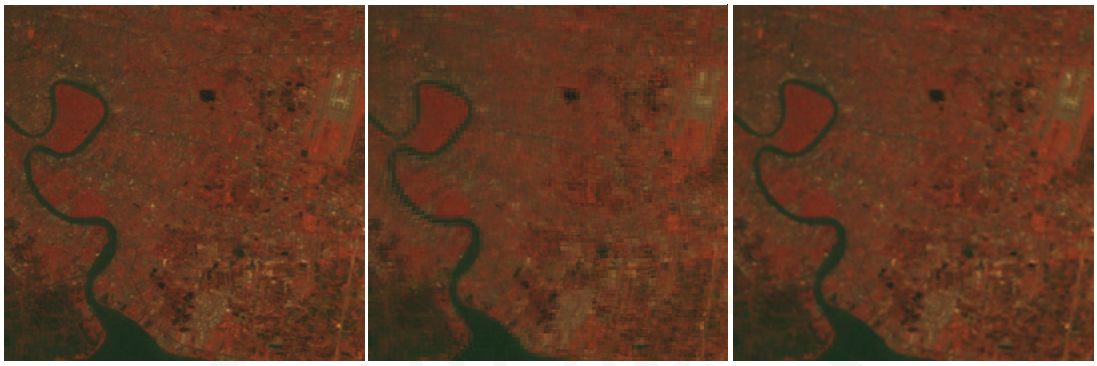

(a) (b) (c)

Figure 45 Comparison fused image (a) fused hyperspectral image without registration error (b) fused hyperspectral image with registration error (c) fused hyperspectral image with registration error using our algorithm

Table 5 Comparison fused image

	x	y	θ	RMSE
fused hyperspectral image without registration error	0	0	0	3.4638
fused hyperspectral image with registration error	-3	-4	-2	5.4734
fused hyperspectral image with registration error using our algorithm	-0.1984	-0.2037	-0.3143	2.6308

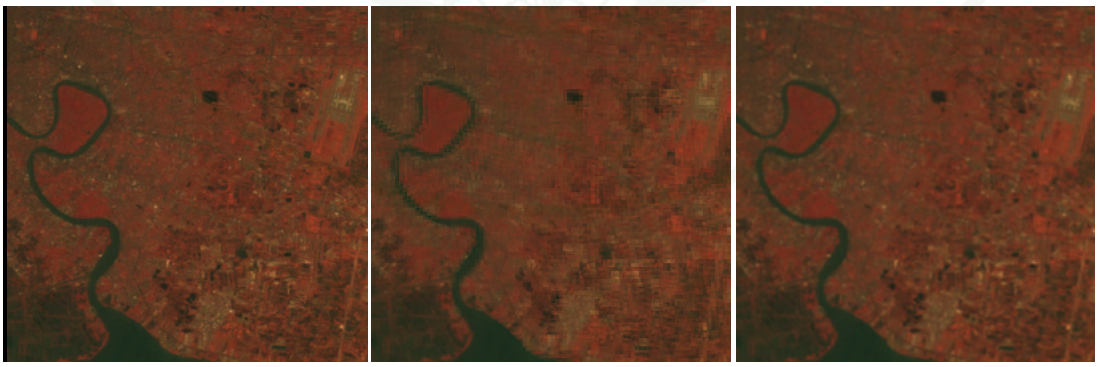

(a) (b) (c)

Figure 46 Comparison fused image (a) fused hyperspectral image without registration error (b) fused hyperspectral image with registration error (c) fused hyperspectral image with registration error using our algorithm

LITERATURE CITED

Aguena, Marcia L.S. and Nelson D.A. Mascarenhas. 2006. Multispectral image data fusion using POCS and super-resolution. vol. 102, pp.178–187. *In* **Computer Vision and Image Understanding**

Carper, W. J., T. M. Lillesand, and R. W. Kiefer. 1990. The use of Intensity–hue–saturation transformations for merging SPOT panchromatic and multispectral image data. vol. 56, no. 4, pp. 459–467. *In* **Photogramm. Eng. Remote Sens.**,

Chavez, P. S. and A. Y. Kwarteng, 1989. Extracting spectral contrast in Landsat thematic mapper image data using selective component analysis. vol. 55, no. 3, pp. 339–348. *In* **Photogramm. Eng. Remote Sens.**

China Centre for Resources Satellite Data and Application. 1991. **Orbital characteristics of CBERS-02B of HJ satellite and Technical specification of payload of HJ-1A**. AvailableSource: http://www.cresda.com/n16/n92006/n92066/n98627/index.html, September 17, 2010.

Chen, C.M. , G.F. Hepner,and R.R. Forster. 2003. Fusion of hyperspectral and radar data using the IHS transformation to enhance urban surface features.vol.58, pp. 19– 30. *In* **ISPRS Journal of Photogrammetry & Remote Sensing**

Chen, S., Q. GUo, H. Leung, and E. Bosse. 2010 A Maximum Likelihood Approach to Joint Image Registration and Fusion. *In* **IEEE Transactions on Image Processing**

Civco, D. L., Y. Wang, and J. A. Silander. 1995. Characterizing forest ecosystems in Connecticut by integrating Landsat TM and SPOT panchromatic data. vol. 2, pp. 216–224. *In* **Proc. ACSM/ASPRS Annu. Conv., Charlotte, NC**.

Elaksher, A. F.. 2008. Fusion of hyperspectral images and lidar-based dems for coastal mapping. vol.46, pp. 493– 498. *In* **Optics and Lasers in Engineering**

Gomez, R. B., A. Jazaeri, and M. Kafatos. 2001. Wavelet-based hyperspectral and multispectral image fusion.vol. 4383, pp.36-42. *In* **Proceedings**

Hardie, R. C., M. T. Eismann and G. L.Wilson. 2004. MAP estimation for hyperspectral image resolution enhancement using an auxiliary sensor. vol.13, no.9, pp.1174-1184. *In* **IEEE Trans. on Image Processing**

Huber, P. J.. Robust Statistics. 1981. **New York: Wiley**

Kay, S. M.. 1993. Fundamentals of Statistical Signal Processing: Estimation Theory. **NJ: Prentice-Hall**

Laben, C. and B. Brower. 2000. Process for enhancing the spatial resolution of multispectral imagery using pan-sharpening. Jan. 4. *In* **U.S. Patent 6 011 875**

Li, S., J. T. Kwok, and Y. Wang. 2002. Using the discrete wavelet frame transform to merge Landsat TM and SPOT panchromatic images. vol. 3, no. 1, pp. 17–23, Mar. *In* **Inf. Fusion**

Li, Z. and H. Leung. 2009. Fusion of Multispectral and Panchromatic Images Using a Restoration-Based Method. vol. 47, no. 5, may. *In* **IEEE TRANSACTIONS ON GEOSCIENCE AND REMOTE SENSING**

Pan, R. and S. J. Reeves. 2006. Efficient Huber-Markov edge-preserving image restoration. vol. 15, no.12. In IEEE Trans. on Image Processing

Segl, K., S. Roessner, U. Heiden, H. Kaufmann. 2003. Fusion of spectral and shape features for identification of urban surface cover types using reflective and thermal hyperspectral data. vol.58, pp. 99– 112. *In* **ISPRS Journal of Photogrammetry & Remote Sensing**

Shettigare, V. K.. 1992. A generalized component substitution technique for spatial enhancement ofmultispectral images using a higher resolution data set., vol. 58, no. 5, pp. 561–567. *In* **Photogramm. Eng. Remote Sens**.

Stoica, P. and Y. Selén. 2004. Cyclic minimizers, majorization techniques, and the expectation-maximization algorithm: A refresher. vol. 21, no. , pp. 112–114. *In* **IEEE Signal Process. Mag.**

Wang, Z. and A. C. Bovik. 1992. A universal image quality index. vol.9, no.3, pp.81-84. *In* **IEEE Signal Processing Letters**

Winkler, G.. 1995. Image Analysis, Random Field and Dynamic Monte Carlo Methods. **New York: Springer-Verlag**

Yifan, Z. and H. Mingyi. 2007. Multi-spectral and hyperspectral image fusion using 3-D wavelet transform. vol.24, no.2, March. *In* **Journal of electronics (China)**

Yuhas, R. H., A. F.H. Goetz, and J. W. Boardman. 1992. Discrimination among semi-arid landscape endmembers using the spectral angle mapper (SAM) algorithm. vol. 92, no. 41, pp 147-149. *In* **Summaries of the 4th JPL Airborne Earth Science Workshop, JPL Publication**

Zhang, Y., S. De Backer, and P. Scheunders. 2008. Bayesian fusion of multispectral and hyperspectral image in wavelet domain. pp 69-72. *In* **Geoscience and Remote Sensing Symposium, 2008. IGARSS 2008. IEEE International**

Zhou, J., D. L. Civco, and J. A. Silander. 1998. A wavelet transform method to merge Landsat TM and SPOT panchromatic data. vol. 19, no. 4, pp. 743–757, Mar. *In* **Int. J. Remote Sens.**

APPENDIX

Appendix Table 1 Spectral bands of the hyperspectral imager sensor from HJ-1A satellite (nm)

Band number	1	2	3	4	5	6	7	8	9	10
begin	459.0	461.1	463.2	465.3	467.5	469.6	471.8	474.0	476.2	478.5
middle	460.0	462.1	464.3	466.4	468.5	470.7	472.9	475.1	477.35	479.6
end	461.1	463.2	465.3	467.5	469.6	471.8	474.0	476.2	478.5	480.7

Appendix Table 1 (Continued)

Band number	11	12	13	14	15	16	17	18	19	20
begin	480.7	483.0	485.3	487.7	490.0	492.4	494.8	497.2	499.7	502.1
middle	481.9	484.2	486.5	488.8	491.2	493.6	496.0	498.4	500.9	503.4
end	483.0	485.3	487.7	490.0	492.4	494.8	497.2	499.7	502.1	504.6

Appendix Table 1 (Continued)

Band number	21	22	23	24	25	26	27	28	29	30
begin	504.6	507.2	509.7	512.3	514.9	517.5	520.1	522.8	525.5	528.3
middle	505.9	508.4	511.0	513.6	516.2	518.8	521.5	524.2	526.9	529.6
end	507.2	509.7	512.3	514.9	517.5	520.1	522.8	525.5	528.3	531.0

Appendix Table 1 (Continued)

Band number	31	32	33	34	35	36	37	38	39	40
begin	531.0	533.8	536.7	539.5	542.4	545.3	548.2	551.2	554.2	557.3
middle	532.4	535.2	538.1	540.9	543.8	546.7	549.7	552.7	555.7	558.8
end	533.8	536.6	539.5	542.4	545.3	548.2	551.2	554.2	557.3	560.3

Appendix Table 1 (Continued)

Band number	41	42	43	44	45	46	47	48	49	50
begin	560.3	563.4	566.6	569.8	573.0	576.2	579.5	582.8	586.2	589.6
middle	561.9	565.0	568.2	571.4	574.6	577.9	581.2	584.5	587.9	591.3
end	563.4	566.6	569.8	573.0	576.2	579.5	582.8	586.2	589.6	593.1

Appendix Table 1 (Continued)

Band number	51	52	53	54	55	56	57	58	59	60
begin	593.1	596.5	600.1	603.6	607.2	610.9	614.6	618.3	622.1	626.0
middle	594.8	598.3	601.8	605.4	609.1	612.7	616.5	620.2	624.0	627.9
end	596.5	600.1	603.6	607.2	610.9	614.6	618.3	622.1	626.0	629.8

Appendix Table 1 (Continued)

Band number	61	62	63	64	65	66	67	68	69	70
begin	629.8	633.8	637.8	641.8	645.9	650.0	654.2	658.4	662.7	667.1
middle	631.8	635.8	639.8	643.8	647.9	652.1	656.3	660.6	664.9	669.3
end	633.8	637.8	641.8	645.9	650.0	654.2	658.4	662.7	667.1	671.5

Appendix Table 1 (Continued)

Band number	71	72	73	74	75	76	77	78	79	80
begin	671.5	676.0	680.5	685.1	689.7	694.5	699.2	704.1	709.0	714.0
middle	673.7	678.2	682.8	687.4	692.1	696.8	701.7	706.5	711.5	716.5
end	676.0	680.5	685.1	689.7	694.5	699.2	704.1	709.0	714.0	719.0

Appendix Table 1 (Continued)

Band number	81	82	83	84	85	86	87	88	89	90
begin	719.9	724.2	729.4	734.7	740.0	745.4	751.0	756.6	762.2	768.0
middle	721.6	726.8	732.0	737.3	742.7	748.2	753.8	759.4	765.1	770.9
end	724.2	729.4	734.7	740.0	745.4	751.0	756.6	762.2	768.0	773.9

Appendix Table 1 (Continued)

Band number	91	92	93	94	95	96	97	98	99	100
begin	773.9	779.8	785.8	792.0	798.2	804.5	810.9	817.5	824.1	830.8
middle	776.8	782.8	788.9	795.1	801.3	807.7	814.2	820.8	827.5	834.3
end	779.8	785.8	792.0	798.2	804.5	810.9	817.5	824.1	830.8	837.7

Appendix Table 1 (Continued)

Band number	101	102	103	104	105	106	107	108	109	110
begin	837.7	844.7	851.7	859.0	866.3	873.7	881.3	889.0	896.9	904.9
middle	841.2	848.2	855.3	862.6	870.0	877.5	885.2	893.0	900.9	909.0
end	844.7	851.7	859.0	866.3	873.7	881.3	889.0	896.9	904.9	913.0

Appendix Table 1 (Continued)

Band number	111	112	113	114	115
begin	913.0	921.3	929.7	938.3	947.1
middle	917.2	925.5	934.0	942.7	951.5
end	921.3	929.7	938.3	947.1	956.0

Appendix Table 2 The values of **A** size of 4x115

	1	2	3	4	5	6	7	8	9	10
1	0.0029	0.0015	0.0037	0.0047	0.0057	0.0106	0.0175	0.0213	0.0226	0.0251
2	0	0	0	0	0	0	0	0	0	0
3	0	0	0	0	0	0	0	0	0	0
4	0	0	0	0	0	0	0	0	0	0

Appendix Table 2 (Continued)

	11	12	13	14	15	16	17	18	19	20
1	0.0312	0.0345	0.0343	0.0367	0.0442	0.0489	0.0500	0.0511	0.0527	0.0586
2	0	0	0	0	0	0	0	0	0	0
3	0	0	0	0	0	0	0	0	0	0
4	0	0	0	0	0	0	0	0	0	0

Appendix Table 2 (Continued)

	21	22	23	24	25	26	27	28	29	30
1	0.0627	0.0631	0.0651	0.0688	0.0703	0.0725	0	0	0	0
2	0	0	0	0	0	0	0.0144	0.0221	0.0175	0.0061
3	0	0	0	0	0	0	0	0	0	0
4	0	0	0	0	0	0	0	0	0	0

Appendix Table 2 (Continued)

	31	32	33	34	35	36	37	38	39	40
1	0	0	0	0	0	0	0	0	0	0
2	0.0143	0.0150	0.0146	0.0146	0.0151	0.0155	0.0157	0.0164	0.0164	0.0169
3	0	0	0	0	0	0	0	0	0	0
4	0	0	0	0	0	0	0	0	0	0

Appendix Table 2 (Continued)

	41	42	43	44	45	46	47	48	49	50
1	0	0	0	0	0	0	0	0	0	0
2	0.0168	0.0171	0.0174	0.0195	0.0225	0.0153	0.0089	0.0396	0.0416	0.0048
3	0	0	0	0	0	0	0	0	0	0
4	0	0	0	0	0	0	0	0	0	0

Appendix Table 2 (Continued)

	51	52	53	54	55	56	57	58	59	60
1	0	0	0	0	0	0	0	0	0	0
2	0.00006	0.0578	0	0	0	0	0	0	0	0
3	0	0	0	0	0	0	0	0	0	0
4	0	0	0	0	0	0	0	0	0	0

Appendix Table 2 (Continued)

	61	62	63	64	65	66	67	68	69	70
1	0	0	0	0	0	0	0	0	0	0
2	0	0	0	0	0	0	0	0	0	0
3	0.0030	0.0257	0.0159	0.0078	0.0307	0.0361	0.0164	0.0314	0.0685	0.0677
4	0	0	0	0	0	0	0	0	0	0

Appendix Table 2 (Continued)

	71	72	73	74	75	76	77	78	79	80
1	0	0	0	0	0	0	0	0	0	0
2	0	0	0	0	0	0	0	0	0	0
3	0.0435	0.0275	0.00005	0.0169	0	0	0	0	0	0
4	0	0	0	0	0	0	0	0	0	0

Appendix Table 2 (Continued)

	81	82	83	84	85	86	87	88	89	90
1	0	0	0	0	0	0	0	0	0	0
2	0	0	0	0	0	0	0	0	0	0
3	0	0	0	0	0	0	0	0	0	0
4	0	0	0	0	0	0	0	0	0.00003	0.0002

Appendix Table 2 (Continued)

	91	92	93	94	95	96	97	98	99	100
1	0	0	0	0	0	0	0	0	0	0
2	0	0	0	0	0	0	0	0	0	0
3	0	0	0	0	0	0	0	0	0	0
4	0.0591	0.0056	0.0028	0.0041	0.0051	0.0052	0.0035	0.0034	0.0074	0.0126

Appendix Table 2 (Continued)

	100	102	103	104	105	106	107	108	109	110
1	0	0	0	0	0	0	0	0	0	0
2	0	0	0	0	0	0	0	0	0	0
3	0	0	0	0	0	0	0	0	0	0
4	0.0221	0.0202	0.0190	0.0258	0.0367	0.0410	0.0259	0.0136	0.0069	0

Appendix Table 2 (Continued)

	111	112	113	114	115
1	0	0	0	0	0
2	0	0	0	0	0
3	0	0	0	0	0
4	0	0	0	0	0

Appendix Table 3 The values of $\boldsymbol{\mu}$ size of 4x1

	1
1	1.5862
2	-1.1605
3	-7.5510
4	-1.9932

Appendix Table 4 The values of $\mathbf{C_1}$ size of 4x4

	1	2	3	4
1	4.9088	3.7701	4.3839	0.4637
2	3.7701	3.8556	4.1065	0.2831
3	4.3839	4.1065	5.3591	0.5914
4	0.4637	0.2831	0.5914	4.4159

CIRRICULUM VITAE

NAME : Mr. Tanakorn Sritarapipat

BIRTH DATE : July 22, 1985

BIRTH PLACE : Chainat, Thailand

EDUCATION :

YEAR	INSTITUTE	DEGREE/DIPLOMA
2008	Kasetsart Univ.	B.Eng. (Electrical Engineering)
2011	Kasetsart Univ.	M.Eng. (Electrical Engineering)

POSITION/TITLE : -

WORK PLACE : -

SCHOLARSHIP/AWARDS : -

PUBLICATIONS : T. Sritarapipat and T. Kasetkasem, "Fusion of Hyperspectral and Multispectral Images using MAP Estimator and Huber-MRF", *ICICTES2011*, Pattaya , Thailand, January 29 - 27, 2011